



REPORT

The Role of Structural Connectivity on Hydraulic Fracture Induced Seismicity – Discrete & Numerical Simulations

Submitted to:

BC Oil & Gas Research & Innovation Society

PO Box 9331 – Stn Prov Govt
Victoria BC V8W 9N3

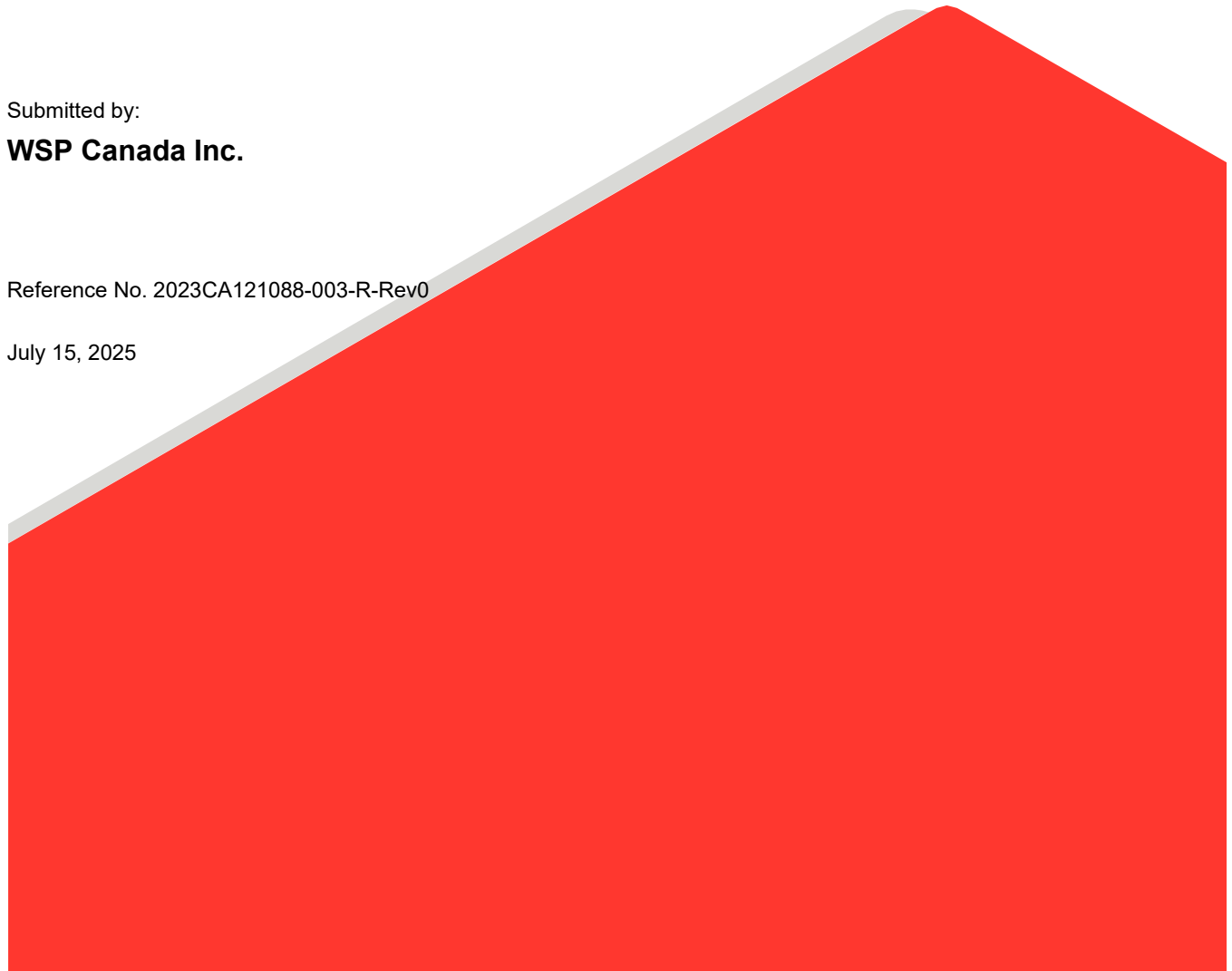
Attention: Richard Slocomb – OGRIS Fund Manager

Submitted by:

WSP Canada Inc.

Reference No. 2023CA121088-003-R-Rev0

July 15, 2025



Distribution List

Electronic Copy: BC Oil & Gas Research & Innovation Society

Electronic Copy: WSP Canada Inc.

Acknowledgements

This work wouldn't have been possible without the support of BC OGRIS and the generous donation of subsurface data by several Montney operators.

Executive Summary

The injection of pressurized fluid into deep reservoirs during hydraulic fracturing, can result in slip on stimulated faults and the generation of seismic energy. This project, following on from a previous study in 2022, has further considered this process by looking at how faults connect to an active well and how pressurised fluid diffuses along this pathway resulting in induced seismicity.

The analysis had two main objectives:

- The characterization, and modelling of the geometry of inferred, reservoir-scale, geological structures and the nature of their connectivity from two adjacent drill pads. This included a novel way of matching the inferred fault geometry using the PEST optimising software controlling the stochastic fault modelling software, FracMan.
- Coupled hydro-mechanical numerical simulation of the pressure diffusion process to validate the underlying conceptual model and test a number of potential mitigation strategies.

The report utilised two primary datasets:

- 2022 Data Set–Open Hole Configuration: This dataset includes seven wells with open hole completions, recording 558 induced seismic events with magnitudes between -0.64 and 3.1. The spatial distribution of events reveals a strongly aligned pattern of seismic lineaments with a broadly NE-SW trend.
- 2024 Data Set–Cased Hole Configuration: This dataset includes wells with plug and perf completions drilled approximately 2.5 km to the southeast, recording significant induced seismicity with a maximum magnitude of 3.1. The spatial distribution of events reveals a strongly aligned pattern of seismic lineaments with a broadly NE-SW trend, very similar the 2022 dataset.

The report provides an analysis of the available datasets, including the spatial distribution of induced seismic events, the length distribution of interpreted induced seismic lineaments, and the distance of events from active wells. The analysis shows that the structural pattern of the Montney reservoir is consistent between the two pads, with a similar pattern of structures being stimulated at this multi-pad scale. In particular, the size distribution of sub-seismic structures were consistent across all of the available data sets including interpreted regional scale seismic structures.

The study utilized DFN models to simulate hydraulic fracture-induced seismicity. The DFN models were optimized using the PEST software to find the best match between observed and simulated seismic events. The analysis revealed that longer hydraulic fractures (open hole completions) result in a larger stimulated volume and increased seismic potential compared to shorter fractures (plug and perf completions). This appears to be driven in part by the longer fractures having an increased probability of intersecting other structures and therefore a greater likelihood of pressure diffusion reaching adversely orientated structures, resulting in slip.

Coupled numerical simulations using the 3DEC version 7.0 (Itasca 2025) software were conducted to validate the conceptual geomechanical model and explore mitigation strategies. The simulations confirmed that seismic events predominantly occur on NE-SW oriented structures. However, pressure was also observed diffusing along NW-SE structures without the generation of any seismicity. This validated one of the underlying concepts of the stochastic DFN simulations, helping to demonstrate this as a significant mechanism in how induced seismicity is triggered.

Several mitigation strategies were tested:

- Lower Injection Rate: Reducing the injection rate to 75% of the base case showed no significant impact on seismicity.
- Slower Ramp Up: Gradually increasing the injection rate, significantly reduced the number of seismic events.
- Hydraulic Fracture Length: Longer fractures resulted in slightly more seismic events.
- Increased Fluid Viscosity: Higher viscosity fluids reduced the number of larger seismic events, focusing seismicity closer to the well.

Key conclusions of the study are:

- The structural pattern of reservoir scale structures within the Montney reservoir studied is consistent across the two different pads, despite being several kilometres apart.
- The combination of the PEST-FracMan software provided an effective way to use stochastic structure modelling to simulate induced seismicity and to subsequently select the most geometric likely case from a large catalogue of equi-probable cases.
- Longer hydraulic fractures did increase the seismic potential.
- Slower ramp-up rates and higher viscosity fluids were seen to provide potentially effective mitigation strategies to reduce induced seismicity.

This report provides valuable insights into the relationship between hydraulic fracturing and induced seismicity, offering practical engineering solutions to mitigate seismic risks in hydraulic fracturing operations.

Study Limitations

WSP Canada Inc. ("WSP") prepared this report solely for the use of the intended recipient, **BC Oil and Gas Research and Innovation Society** (BCOGRIS), in accordance with the professional services agreement between the parties. In the event a contract has not been executed, the parties agree that the WSP General Terms for Consultant shall govern their business relationship which was provided to you prior to the preparation of this report.

The report is intended to be used in its entirety. No excerpts may be taken to be representative of the findings in the assessment.

The conclusions presented in this report are based on work performed by trained, professional and technical staff, in accordance with their reasonable interpretation of current and accepted engineering and scientific practices at the time the work was performed.

The content and opinions contained in the present report are based on the observations and/or information available to WSP at the time of preparation, using investigation techniques and engineering analysis methods consistent with those ordinarily exercised by WSP and other engineering/scientific practitioners working under similar conditions, and subject to the same time, financial and physical constraints applicable to this project.

WSP disclaims any obligation to update this report if, after the date of this report, any conditions appear to differ significantly from those presented in this report; however, WSP reserves the right to amend or supplement this report based on additional information, documentation or evidence.

WSP makes no other representations whatsoever concerning the legal significance of its findings.

The intended recipient is solely responsible for the disclosure of any information contained in this report. If a third party makes use of, relies on, or makes decisions in accordance with this report, said third party is solely responsible for such use, reliance or decisions. WSP does not accept responsibility for damages, if any, suffered by any third party as a result of decisions made or actions taken by said third party based on this report.

WSP has provided services to the intended recipient in accordance with the professional services agreement between the parties and in a manner consistent with that degree of care, skill and diligence normally provided by members of the same profession performing the same or comparable services in respect of projects of a similar nature in similar circumstances. It is understood and agreed by WSP and the recipient of this report that WSP provides no warranty, express or implied, of any kind. Without limiting the generality of the foregoing, it is agreed and understood by WSP and the recipient of this report that WSP makes no representation or warranty whatsoever as to the sufficiency of its scope of work for the purpose sought by the recipient of this report.

In preparing this report, WSP has relied in good faith on information provided by others, as noted in the report. WSP has reasonably assumed that the information provided is correct and WSP is not responsible for the accuracy or completeness of such information.

Benchmark and elevations used in this report are primarily to establish relative elevation differences between the specific testing and/or sampling locations and should not be used for other purposes, such as grading, excavating, construction, planning, development, etc.

This limitations statement is considered an integral part of this report.

Table of Contents

EXECUTIVE SUMMARY iii

STUDY LIMITATIONS v

1.0 INTRODUCTION 1

2.0 AVAILABLE DATASETS 2

2.1 2022 Data Set–Open Hole Configuration 2

2.2 2024 Data Set–Cased Hole Configuration 3

2.3 Available Seismic Faults at the Wabamun Horizon 6

2.3.1 Length Distribution of Interpreted Induced Seismic Lineaments 7

2.3.2 Distance of Events from Active Wells 2022 & 2024 10

2.3.3 Magnitude Distribution 2022 & 2024 11

2.3.4 Data Set Comparison Summary 12

3.0 STOCHASTIC SIMULATION OF HYDRAULIC FRACTURE INDUCED SEISMICITY 14

3.1 DFN Model Description 14

3.2 Fault Network Optimisation 15

3.3 Selection of Best Matched Scenarios 16

3.4 Stochastic Simulation Summary 18

3.5 Using the DFN Model to Evaluate the Impact of Frac Length 19

3.6 DFN Summary 25

4.0 NUMERICAL SIMULATION OF HYDRAULIC FRACTURE INDUCED SEISMICITY 26

4.1 Introduction 26

4.2 Model Construction 26

4.3 Model Parametrisation 29

4.4 Model Initialisation and Computation 31

4.5 Model Results 32

4.5.1 Base Case Simulations 33

4.5.2 Base Case Summary 37

| | | |
|------------|---------------------------------------|-----------|
| 4.5.3 | Mitigation Cases..... | 38 |
| 4.5.4 | Lower Injection Rate | 38 |
| 4.5.5 | Hydraulic Fracture Length Cases | 39 |
| 4.5.6 | Slower Ramp up..... | 40 |
| 4.5.7 | Increased Viscosity | 43 |
| 4.6 | Summary of Numerical Assessment..... | 45 |
| 5.0 | SUMMARY | 48 |
| 6.0 | CLOSURE | 50 |
| | REFERENCES | 52 |

TABLES

| | |
|--|----|
| Table 1: Distance to Event Data for the 3 Induced Seismic Data Sets | 11 |
| Table 2: Summary of Key Input Parameters, Ranges and Optimised Estimate from 2022 and 2024 | 16 |
| Table 3: Summary of In Situ Stress..... | 29 |
| Table 4: Summary of Rock and Fluid Properties..... | 29 |
| Table 5: Summary of Joint Mechanical and Hydraulic Properties..... | 29 |
| Table 6: Fluid Pumping Scheme | 30 |
| Table 7: Base Case and 5 Different Ramps up Scenarios..... | 42 |
| Table 8: Viscosity Cases | 43 |

FIGURES

| | |
|--|---|
| Figure 2-1: Plan View and Section View of Induced Seismic Events for OP3; Size Scaled by Magnitude (max magnitude M=3.1) and Coloured by the Wells they are Associated with. Section View Shows Major Stratigraphic Surfaces and the Lower Montney Wells. | 2 |
| Figure 2-2: Plan View and Section View of Induced Seismic Events for the 2024 data set; Size Scaled by Magnitude (Max Magnitude M=3.1) | 4 |
| Figure 2-3: Plan View and Section View of Induced Seismic Events for the 2024 Data Set Associated with Well_1; Size Scaled by Magnitude (Max Magnitude M=3.1) | 5 |
| Figure 2-4: Raster Based Image of Interpreted TGS Seismic Faults at the Wabamun Level..... | 6 |
| Figure 2-5: Size and Orientation Properties of the TGS Seismic Faults from the Wabamun Horizon. a) Histogram of all Fault Lengths. b) Rose Diagram of all Faults. c) Rose Diagram of all Faults < 1000 m. d) Rose Diagram of all Faults < 500 m | 7 |

| | |
|--|----|
| Figure 2-6: Interpreted Seismic Lineaments from the 2022 and 2024 Data Sets, also showing the Sub-regions used to Analyse the Data, along with Properties of the Sub-areas Summarised in the Inset Table..... | 8 |
| Figure 2-7: Power Law Plot Showing the Size Distribution Curves for the 2022 Data Set (North) and 2024 Data Set (East, Central, West, Central West Sub-areas) | 9 |
| Figure 2-8: Power Law Plot Showing the Size Distribution Curves for the 2024 Data Set (East) and the Interpreted TGS Seismic Faults, Showing the Same Gradient and a Similar Overall Intensity..... | 9 |
| Figure 2-9: 2022 (Open Hole, Top Left) and 2024 (Cased hole, Bottom Right) Events Coloured by Distance to Well | 10 |
| Figure 2-10: Distribution of Distance of Induced Events from Active Well for Open Hole (left) and Cased Hole (centre) Stimulation and Plotted Together as a CDF Plot (right)..... | 11 |
| Figure 2-11: Distribution of Seismic Magnitude Response for the Open Hole (2022) and Cased Hole (2024) Completions | 12 |
| Figure 3-1: (b) Connected fractures (red) with Simulated (red) and Observed (green) Induced Seismicity. (C) Mohr's Circle Illustrating Fault Orientations that are Prone to Seismicity due to an Oblique Orientation to σ_H . The Three Fracture Sets are Annotated along with Diagrams of Failure Modes for the Tension, Seismogenic, and Aseismic Regions of the Mohr's Circle..... | 14 |
| Figure 3-2: The PEST Workflow for Estimating the Best DFN Model | 15 |
| Figure 3-3: Workflow for Selecting Optimum PEST Realisation. a) 250 × 250 m Grid, b) Observed Faults Mapped into the grid, c) Simulated Faults (One Realisation) Mapped into the Grid, and d) Product of Two Grids where Observed and Simulated Agree..... | 17 |
| Figure 3-4: Best Two Realizations Selected for the 3DEC Numerical Analysis..... | 18 |
| Figure 3-5: Simulated Hydraulic Fracture Length. a) 150 m Full Length Hydraulic Fractures at Perf Centres, b) 600 m Full Length Hydraulic Fractures at Perf Centres, and c) 600 m Full Length Hydraulic Fractures, One Frac Per Stage | 19 |
| Figure 3-6: Realisations 1-4 (or 5) Showing the Connected Fractures (Stimulated Volume) for 150 m Long Hydraulic Fractures. Grid Squares are 2000 × 2000 m | 21 |
| Figure 3-7: Realisations 1-4 (or 5) Showing the Connected Fractures (Stimulated Volume) for 600 m Long Hydraulic Fractures. Grid Squares are 2000 × 2000 m | 22 |
| Figure 3-8: Density Plot of Fracture Count from Compiling 50 Realisations of the Connected Fracture Results for Top) 150 m Long Hydraulic Fractures, and 600 m Long Hydraulic Fractures. Red Grid Cells are 2000 × 2000 m | 23 |
| Figure 3-9: Distribution of the Distance from Active Stages to Connected Fractures. Left) 150 m Frac Lengths, Centre) 600 m Frac Length and Right) Cumulative Frequency Distribution (CDF) for the 2 Models..... | 24 |
| Figure 3-10: (Left CDF of Connected Fracture Count for the 150 m and 600 m Frac Models; and left) CDF of Connected Fracture Area for the 150 m and 600 m Frac Models | 25 |
| Figure 4-1: Development of DFN Derived Structural Model into 3DEC Ready Model. a) Red Lines Represent the Best Matched Connected Fault Network. b) Original Hydraulic Fractures in DFN Analysis used Tightly Spaced Fracs for Each Perf. c) The Final Model Replaces the Perf Clusters with Single Frac Per Stage to make the Analysis Simpler | 27 |

| | |
|--|----|
| Figure 4-2: Conversion of the DFN Model into a 3DEC Model. Upper Image shows the Connected Fractures (Both Hydraulic Fracs and Faults), and the Lower Image shows the Completed Model Imbedded within the 3DEC Model..... | 28 |
| Figure 4-3: Modified Injection Stages to Reduce Simulation Time. 18 Original Stages (Purple) Reduced to 10 (Red) | 30 |
| Figure 4-4: Contour Plots for In Situ Pore Pressure, Maximum and Minimum Principal Stress After Initial Equilibrium (before Fluid Injection)..... | 32 |
| Figure 4-5: Pore Pressure Distribution at the End of Stage 2, 4, 6, 8 and 10 for the Base Case. The Small Black Dots on the Hydraulic Fractures Represent the Injection Points | 35 |
| Figure 4-6: Pore Pressure History Graphs at the End of Stage 10 for the Base Case | 35 |
| Figure 4-7: Induced Seismicity at the End of Stage 10 of Injection for the Base Case. Top: all Seismic Events; Bottom: Positive Magnitudes..... | 36 |
| Figure 4-8: Histogram of Moment Magnitude for the Base Case (Left) and Field Data (Right) | 37 |
| Figure 4-9: Comparison of Measured (Field) and Simulated Seismic Magnitudes. The Left Plot shows the Full Modelled Range, and the Right Plot shows the Modelled Data Clipped to the Minimum Measured Value, Magnitude Zero | 37 |
| Figure 4-10: Comparison of Seismicity Distribution for the Base Case (Left) and Lower Injection Rate (Right)..... | 38 |
| Figure 4-11: Comparison between the Base Case Model (125 m Long Fracs) and Extended Frac Model (300 m Long Fracs)..... | 39 |
| Figure 4-12: Comparison between the Seismicity for the Base Case Models (125 m Long Fracs) and Extended Frac Model (300 m Long Fracs)..... | 40 |
| Figure 4-13: The Concept of Flux vs Injection Duration for the Ramp-up Scenarios..... | 41 |
| Figure 4-14: Ramp-up Rates and Pumping Durations | 41 |
| Figure 4-15: Comparison of Seismicity Distribution for the Base Case and 5 Different Ramp up Scenarios | 43 |
| Figure 4-16: Comparison of the Induced Seismicity Distribution for the Base Case and 2 Different Viscosity Scenarios | 45 |
| Figure 4-17: Comparison of Seismicity Distribution for the Base Case and 2 Different Viscosity Scenarios. Modelled Magnitudes only Displayed about Magnitude..... | 45 |
| Figure 4-18: The Comparison of the Number of Events in Each Scenario | 46 |
| Figure 4-19 The comparison of the Largest Magnitude in Different Scenarios..... | 46 |
| Figure 4-20: Summary of Seismicity Distribution for the Base Case and all other Scenarios | 47 |

1.0 INTRODUCTION

Pressurized fluid, injected into deep gas reservoirs during hydraulic fracturing, changes the effective stresses on faults that may cause slip, releasing energy as earthquakes. This project extended work done during 2022/23 to further understand this process by considering the injection of high-pressure fluid into the subsurface; the diffusion of pressure and fluid away from the well completion; the stresses and pore pressures in the ground; the faults that may be reactivated; and whether there are ways to mitigate the occurrence of induced seismicity.

Previously WSP had gained access to operator datasets from the KSMMA where a range of events have been observed. This previous project allowed the characterisation of aspects of the underlying structural pattern of sub-seismic structures that were interpreted as carrying pressure away from the well, resulting in the reactivation of critically stressed structures. Access to an additional set of data, from an adjacent pad to the first one, allows us to improve the structural characterisation and further understand how pressure is diffusing through the reservoir away from the well. This work builds on the FracMan DFN simulation workflow, developed in the initial project. As these two adjacent pads have used contrasting completion styles, one being open holed and the other a cased hole completion, there was an opportunity to investigate how completion style impacts the distribution of induced events. With similar structural patterns and geomechanical setting, this provided a useful examination of this aspect of the hydraulic fracturing process and how it impacts induced seismicity. Our overall goal remains to find practical engineering solutions to the mitigation issue that can be readily applied by operators that would result in minimum loss of resource.

The main objectives of this study are therefore:

- Improved structural characterisation of Montney reservoir structures and understanding of their distribution.
- Comparison between open hole and cased completion stimulations in a very similar rock mass, and whether there is a material difference in the induced seismicity in the studied setting.
- To improve understanding of potential mitigation approaches.

The initial project during 2022/3 demonstrated the critical role of conductive structures carrying fluid and pressure away from the well, resulting in the reactivation of structures at distance from the injection points (Rogers & McKean 2022). With the securing of the additional data set from a pad adjacent to the previously studied pad, this project has provided an opportunity to better characterise the pattern of subsurface structures, critical for both conducting pressure as well as the seismicity generation.

The previous analysis used an unconditioned stochastic modelling approach to reproduce realistic structural patterns in the subsurface. Improvements in the approach using an inverse modelling approach, allow the generation of the most likely subsurface description of structures (McKean et al 2024). Based upon this structural modelling we have investigated critical differences between how the open hole and cased hole completions, connect with subsurface structures and how the seismicity distributes away from the well.

Building on these high-fidelity structural DFN models, 3DEC® models considering both open hole and cased completions, have been used to numerically simulate induced seismicity. The goal of the modelling is to investigate if the completion style makes any material impact upon the induced seismicity and whether any of the available stimulation properties might result in less seismicity.

2.0 AVAILABLE DATASETS

2.1 2022 Data Set–Open Hole Configuration

The data set for Operator 3 is derived from the treatment of seven wells, four completed in the Upper Montney and three in the Lower Montney (A2, A4, and A6). An open hole slickwater completion with ~50 m long stages were undertaken over two separate time periods (Phase 1 and Phase 2, separated by approximately 9 months). A total of 558 of induced seismic events were recorded by an operator-owned shallow buried array, with moment magnitudes between -0.64 and 3.1 observed. Induced events have been associated with the active stages from the wells using a simple temporal filter, Figure 2-1.

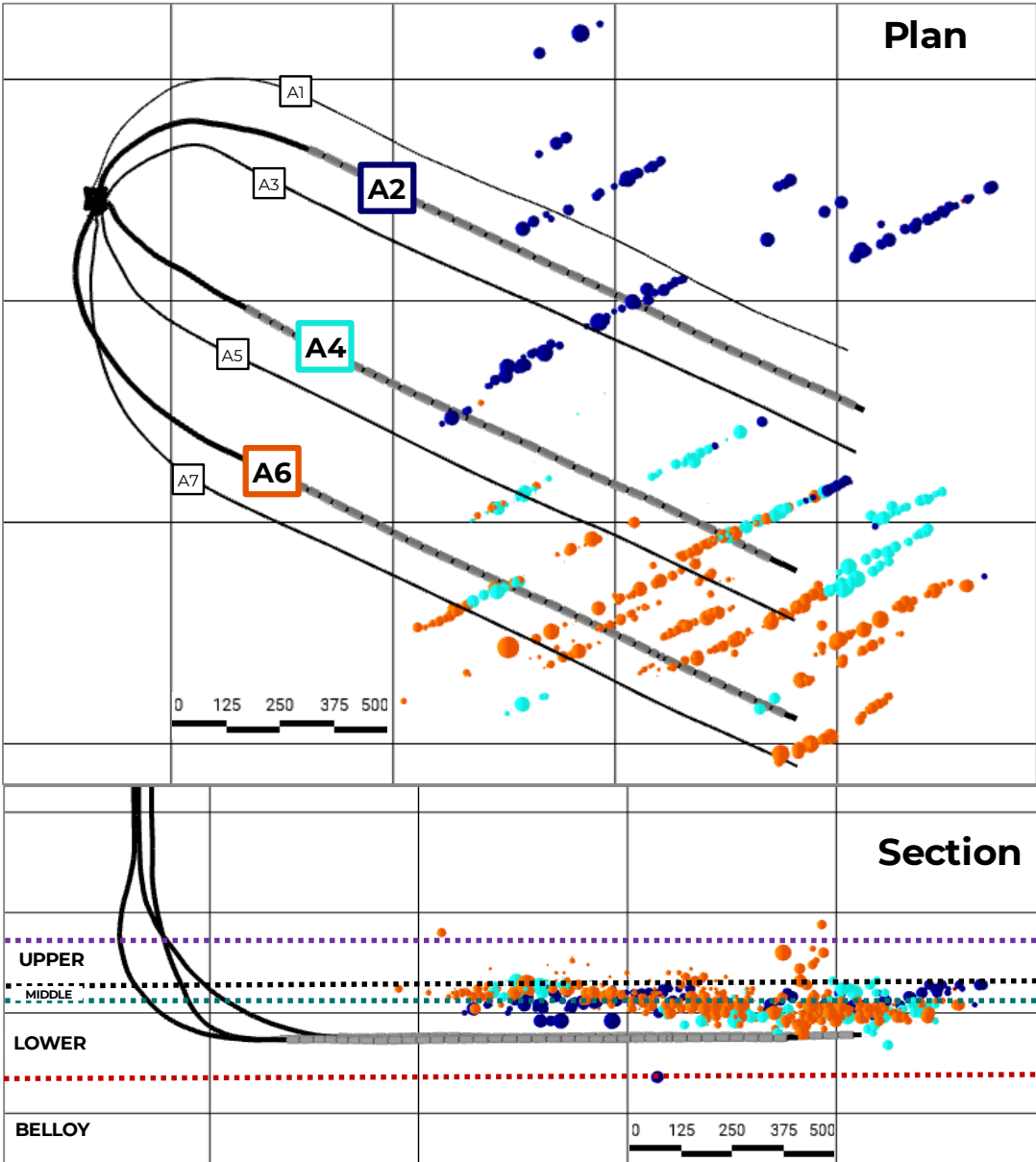


Figure 2-1: Plan View and Section View of Induced Seismic Events for OP3; Size Scaled by Magnitude (max magnitude M=3.1) and Coloured by the Wells they are Associated with. Section View Shows Major Stratigraphic Surfaces and the Lower Montney Wells.

The spatial distribution of events reveals a strongly aligned pattern of seismic lineaments with a broadly NE-SW (060 deg) trend. The events are spread across the 3 lower wells and extend up to ~600 m away from the active wells, with most of the events being clustered in the toe half of the wells. These data are presented in Section 2.3.2.

The shallow array geometry results in significantly more vertical uncertainty than horizontal. However, analysis of when the seismicity occurred relative to which wells were active, allows us to conclude that the induced seismicity is predominantly within the Lower Montney and Debolt Formation. However, we do acknowledge that there is some seismicity associated with Upper Montney stimulation. This may be leakage of pressure from Upper Montney wells down into the Lower Montney, a failure of the temporal filter to accurately associate stage activity with the correct events or other causes.

2.2 2024 Data Set–Cased Hole Configuration

The 2024 data set represents an 8 well pad, drilled approximately 2 km to the south of the 2022 data set. The wells on this pad were completed using a plug and perf completion style and are referred to as a cased hole completion, in contrast to the 2022 wells being open hole completion. As expected, the depth accuracy of the induced events isn't high. However, the majority of the seismicity is associated with the 2 wells drilled in the Lower Montney (Well_1, Well_2), consistent with the 2022 data set observations. The maximum magnitude recorded here is 3.1, the same as seen to the north.

The spatial distribution of events reveals a strongly aligned pattern of seismic lineaments with a broadly NE-SW (060 deg) trend. The events are spread across the 2 Lower Montney wells (Well_1, Well_2) and extend laterally up to ~1500 m away from the active wells. These data are presented in Section 2.3.2.

For the purposes of this study, the primary focus has been on the induced events associated with the stimulation of Well_1, Figure 2-2, Figure 2-3. Stimulation of the Well_1 resulted in significant induced seismicity. Initial attempts to mitigate the seismicity were from skipping stages. An initial 4 stages were stimulated, with a stage skipped. Then two more stimulated and a stage skipped. Then three more stimulated followed by 3 stages skipped. This was followed by three more stimulated, three skipped, and a final five more stimulated. Then treatment was finally abandoned after a total of 18 active stages. Each stage had 6-8 perf clusters (2-3 perfs per cluster), with an estimated frac half length in the range of 75 – 150 m. It was not believed that the well directly intersected any of the structures illuminated by the induced seismicity. During reaming of the well, prior to treatment, no displacements were observed in the wellbore. Therefore, it is concluded that connection from the well to any seismogenic faults was either through the hydraulic fractures or non-seismogenic faults.

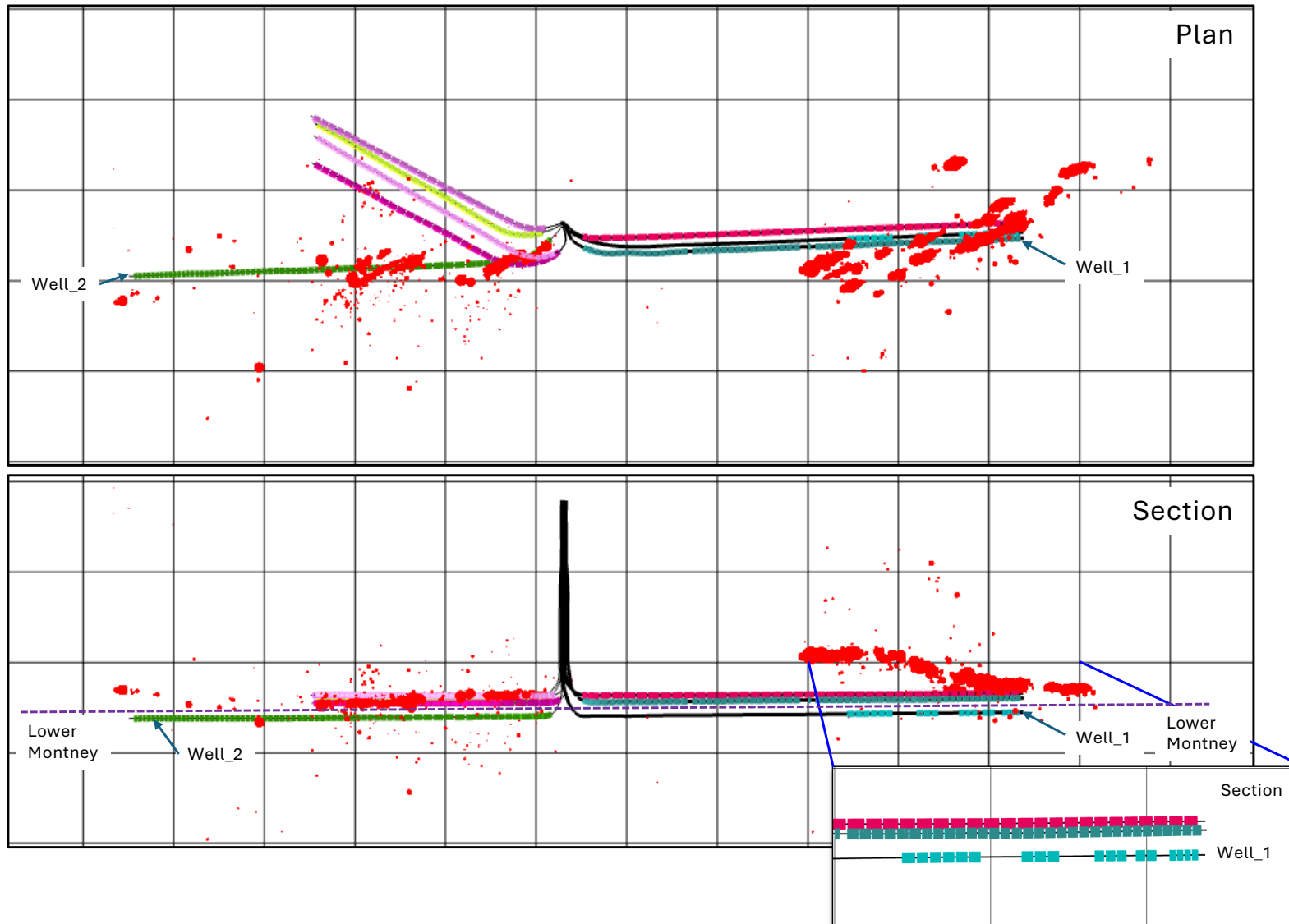


Figure 2-2: Plan View and Section View of Induced Seismic Events for the 2024 data set; Size Scaled by Magnitude (Max Magnitude M=3.1)

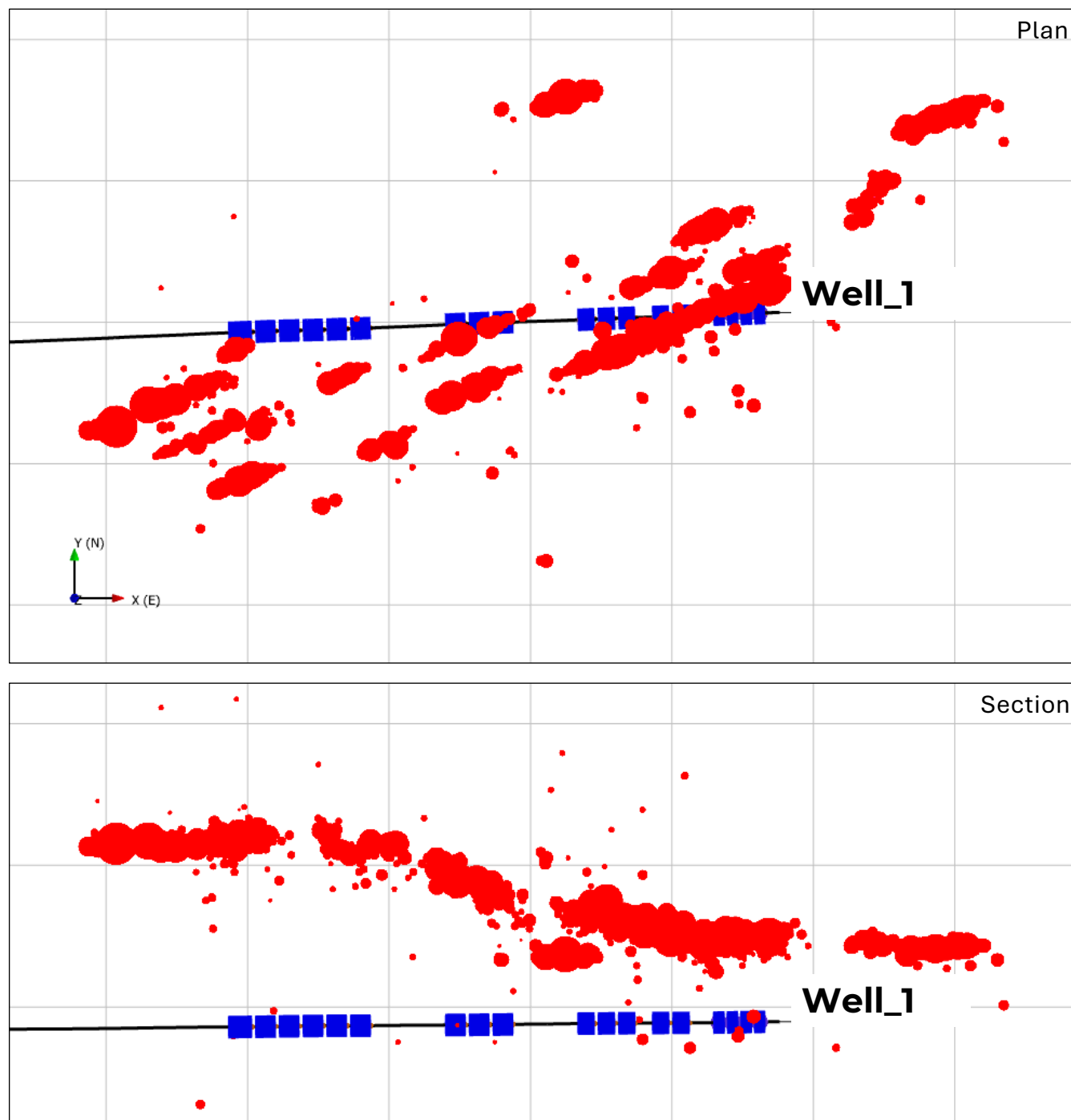


Figure 2-3: Plan View and Section View of Induced Seismic Events for the 2024 Data Set Associated with Well_1; Size Scaled by Magnitude (Max Magnitude M=3.1)

2.3 Available Seismic Faults at the Wabamun Horizon

Interpreted seismic faults from the Devonian Wabamun horizon were available from the area to the south of the 2024 data set and encompassing the 2024 data set and extending to the west and south. These deeper Devonian faults are believed have some expression at the Triassic Montney level. This data is owned by TGS and WSP were granted a licence to see, but not directly reproduce these faults. To give an indication of these faults, their intensity (P32) has been mapped into grid with cells 250 × 250 m, Figure 2-4.

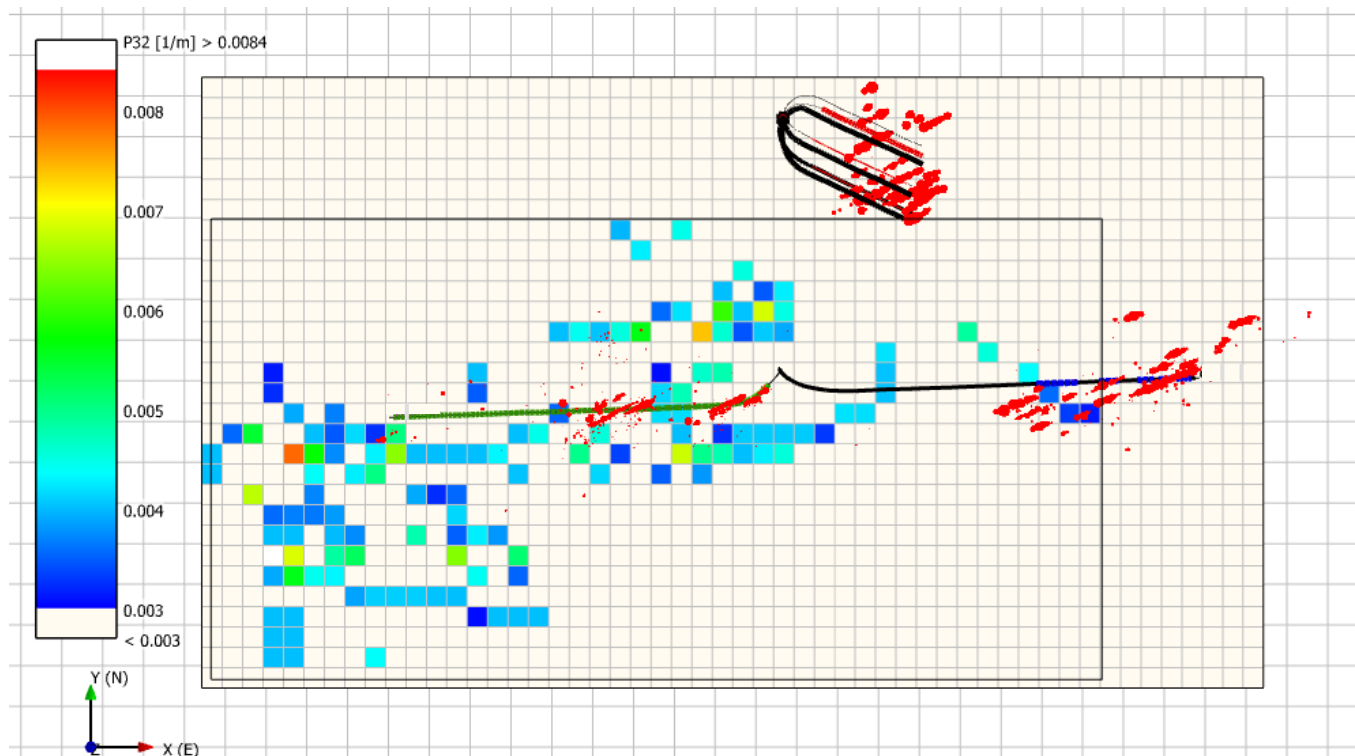


Figure 2-4: Raster Based Image of Interpreted TGS Seismic Faults at the Wabamun Level

Analysis of the length and orientation (strike) of these faults has been carried out, with these results shown in Figure 2-5.

There are a number of observations we can draw from this analysis:

- The interpreted faults extend up to approximately 4500 m long although 85 percent of the fault lengths are less than 1000 m, broadly the same the length imaged by the induced seismic lineaments. Whilst 4500 m might be the longest interpreted fault, it is unlikely that that represent a single continuous structure and is most likely comprised a series of discrete fault segments with varying degrees of connectivity.
- The largest faults show a broadly east-west trend and are believed to be associated with the Fort St John graben to the north.
- However, as we filter out the longer structures, the ENE-WSW (set 1) and ESE-WNW (set 2) structures become more common. Set 1 is the seismogenic trend observed in both the 2022 and 2024 data sets and Set 2 is the inferred aseismogenic fault set required to ensure connectivity between the wells and more distal seismogenic structures.

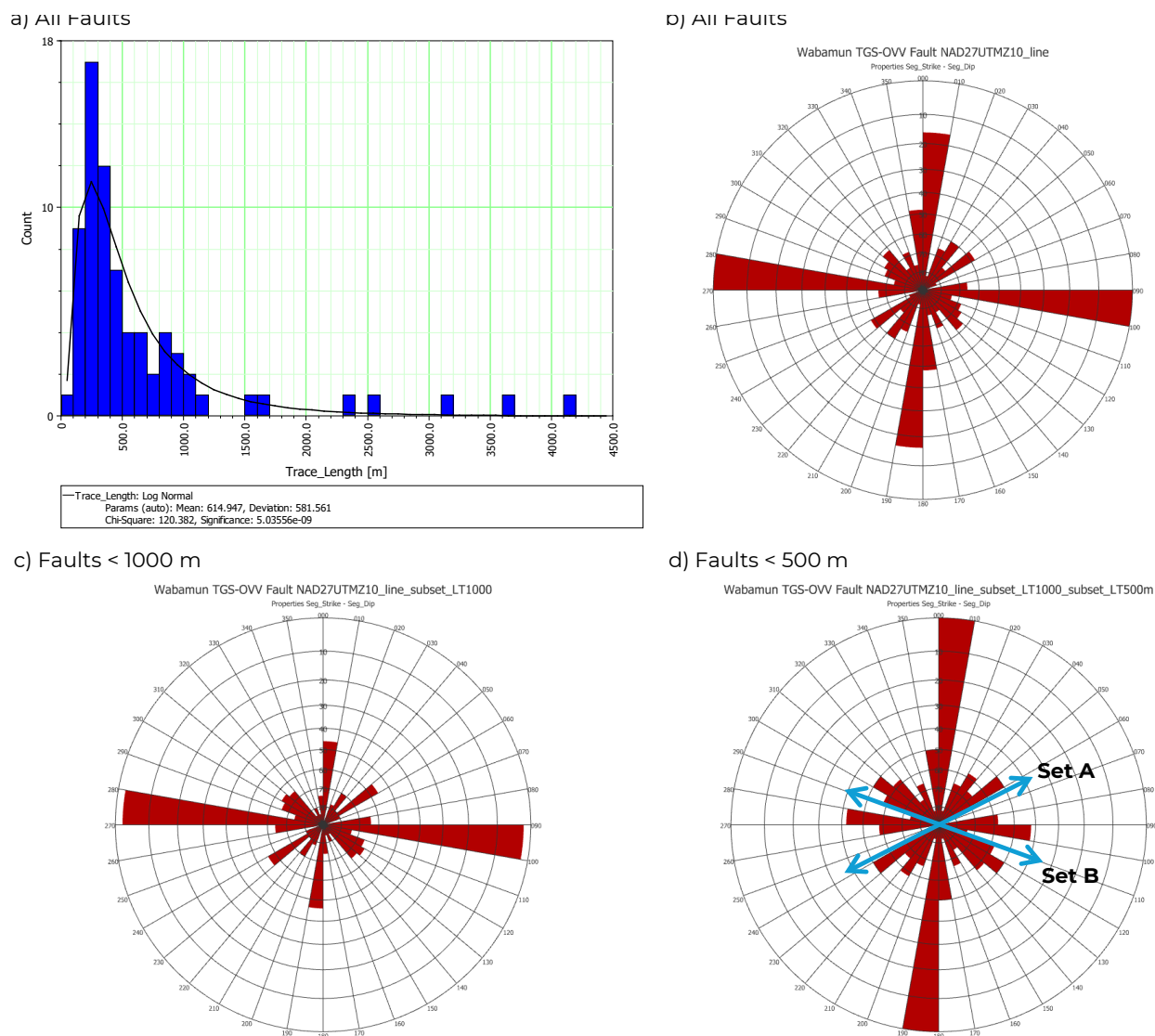


Figure 2-5: Size and Orientation Properties of the TGS Seismic Faults from the Wabamun Horizon.

a) Histogram of all Fault Lengths. b) Rose Diagram of all Faults. c) Rose Diagram of all Faults < 1000 m. d) Rose Diagram of all Faults < 500 m

2.3.1 Length Distribution of Interpreted Induced Seismic Lineaments

For both the 2022 and 2024 data sets, the length of interpreted seismic lineaments has been compared. Lineaments are interpreted by digitising the inferred length as seen from the distribution of induced seismic events. It is likely that this method does have some inaccuracy in length determination. The approach may slightly under-represent the length as there is a reduced chance of pressure diffusion occurring at the tips of the structures. Conversely, it is possible that whilst pressure is diffusing along the structures as indicated by the observed seismic induced events, those features may comprise multiple fault segments rather than a single uninterrupted fault element. However, given these uncertainties, it is believed these measurements represent a reasonable estimate of overall structure length. Interpreted lineaments from the two data sets are shown in Figure 2-6, also showing the 5 sub-groups that they have been grouped into.

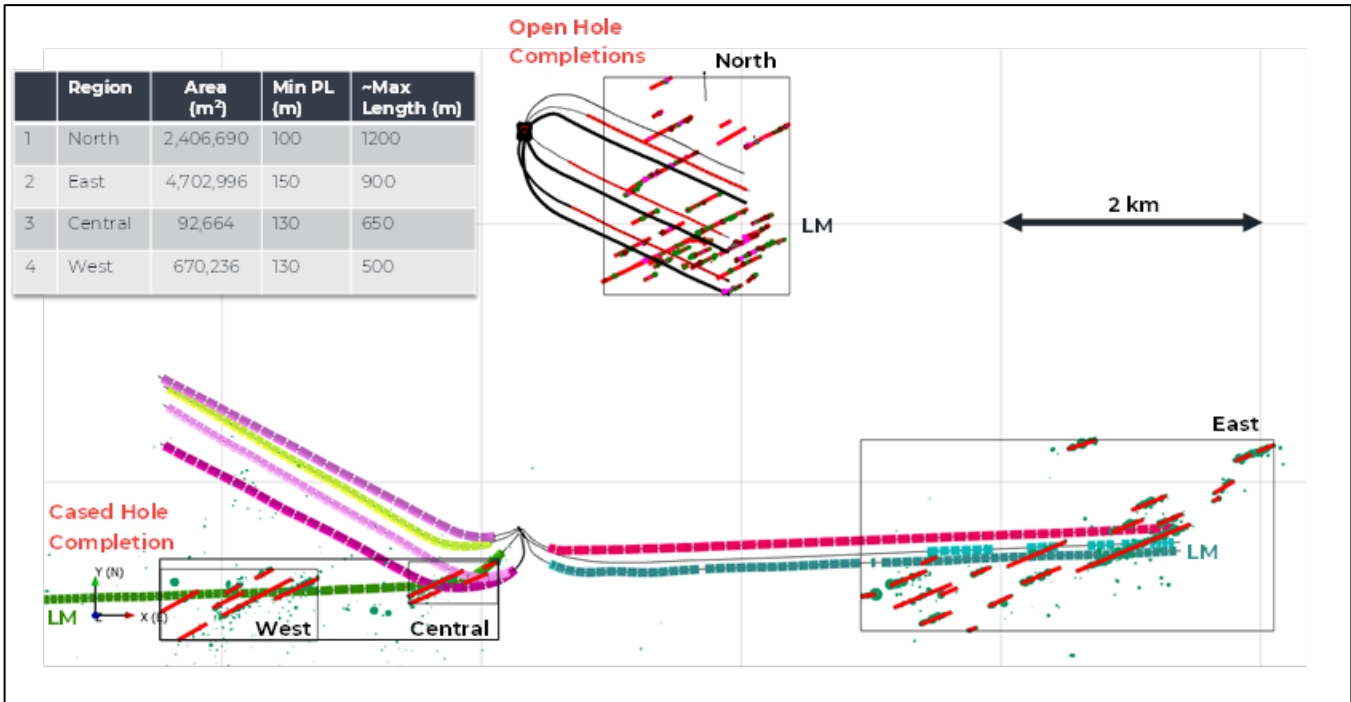


Figure 2-6: Interpreted Seismic Lineaments from the 2022 and 2024 Data Sets, also showing the Sub-regions used to Analyse the Data, along with Properties of the Sub-areas Summarised in the Inset Table

The length data for the induced seismic lineaments have been plotted on power law plots which show the length of structure plotted against the reverse cumulative count of structures, normalised by the area of each of the sub-areas. The curves are interpreted to find the straight-line segment of each data set, with the equation of the best fit line shown alongside the curves in Figure 2-7. Remarkably all of the different areas show the same gradient (-1) that was seen in the original work on the 2022 data set (North area).

The relative height position of the lines in Figure 2-7 are related to the intensity of faults within the demarked areas. Where the area is large relative to the mapped faults, the line will be lower as the normalisation area is larger (e.g., East area). Where the area is small relative to the mapped faults, the line will be higher as the normalisation area is small (e.g., Central area). Regardless of the relative location of the interpreted power law lines, the fact that they all show the same gradient, strongly suggests that the structural pattern illuminated by hydraulic fractured induced pore pressure changes seen within the 2022 and 2024 data sets are very similar, despite the >2 km offset.

This work has been extended to include the addition of the major interpreted TGS seismic faults to the size analysis, Figure 2-8. This shows that the power law gradient of the induced seismic lineament size and the interpreted TGS seismic faults is almost identical. The relative intensity is close although defining the appropriate normalisation area for the data sets is challenging. However, this relationship strongly indicates that the induced seismic lineaments are the small-scale expression of the larger interpreted TGS seismic faults.

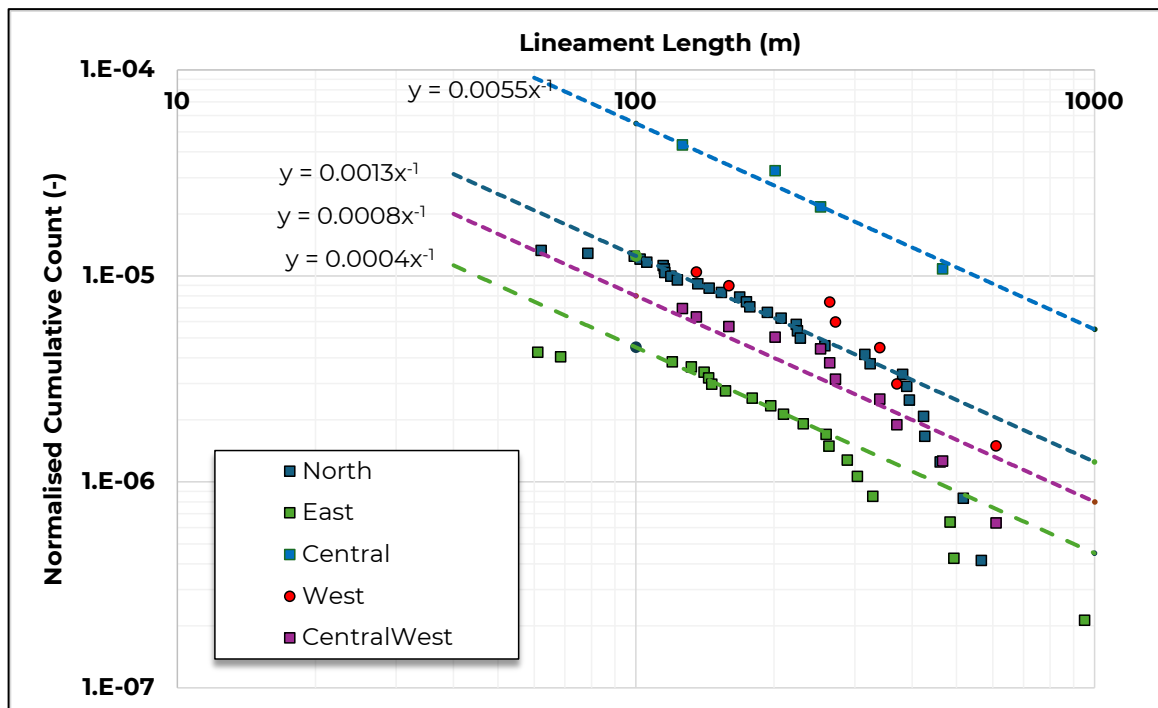


Figure 2-7: Power Law Plot Showing the Size Distribution Curves for the 2022 Data Set (North) and 2024 Data Set (East, Central, West, Central West Sub-areas)

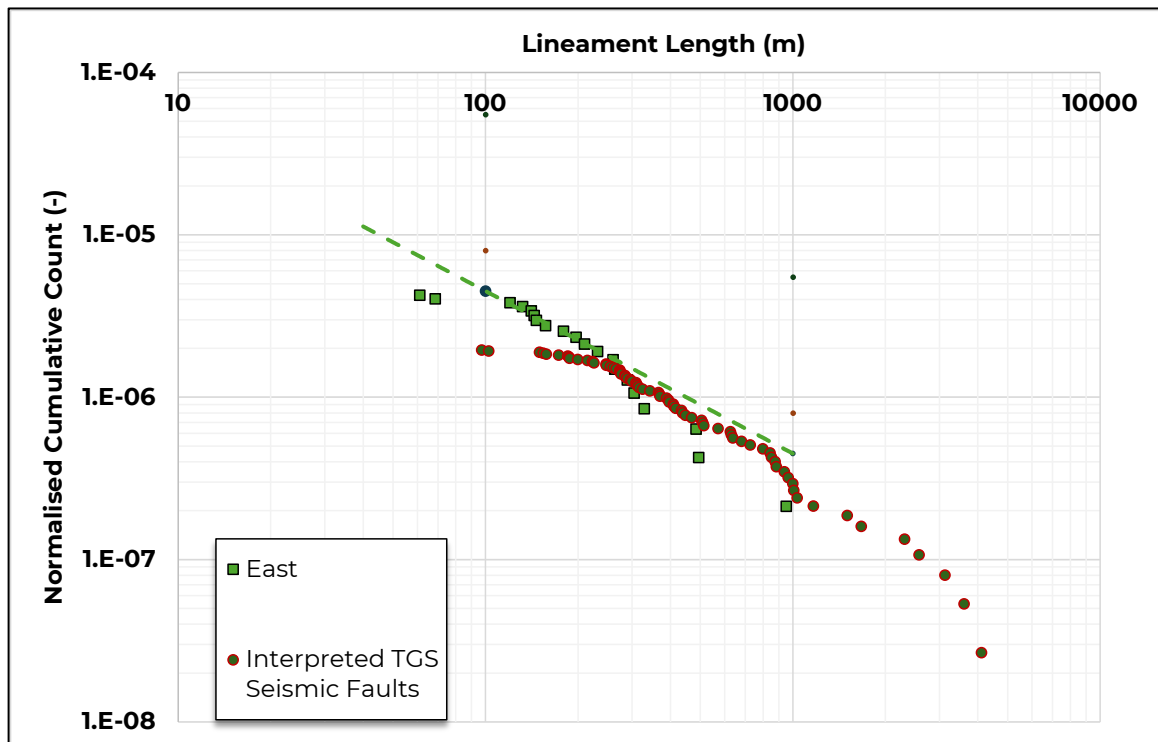


Figure 2-8: Power Law Plot Showing the Size Distribution Curves for the 2024 Data Set (East) and the Interpreted TGS Seismic Faults, Showing the Same Gradient and a Similar Overall Intensity

2.3.2 Distance of Events from Active Wells 2022 & 2024

The distance of induced events from the active wells has been reviewed for the two data sets, see Figure 2-9. Histograms of distance of events from the active stages are shown in Figure 2-10. This shows that over the first 500 m, the two data sets are broadly similar. However, the cased hole completions did stimulate events up to ~1,500 m in comparison to the ~600 m for the open hole completions. Note that these distances represent the distance from events to the nearest active stage, not necessarily the active stage that resulted in the event. The actual distance could therefore be a farther.

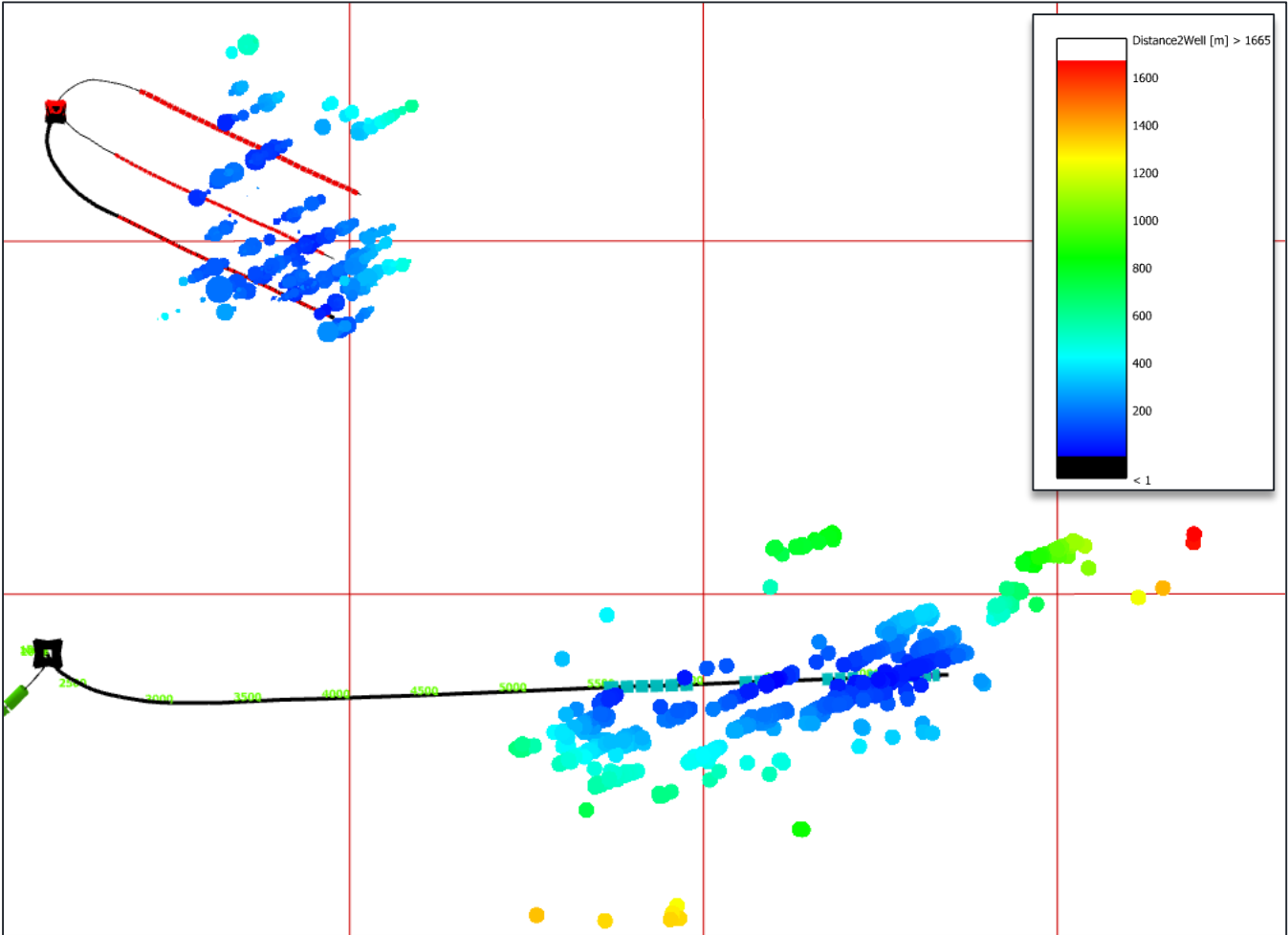


Figure 2-9: 2022 (Open Hole, Top Left) and 2024 (Cased hole, Bottom Right) Events Coloured by Distance to Well

Best fit distributions for the radial distance measurements for the 2022 and 2024 data sets are shown in Table 1.

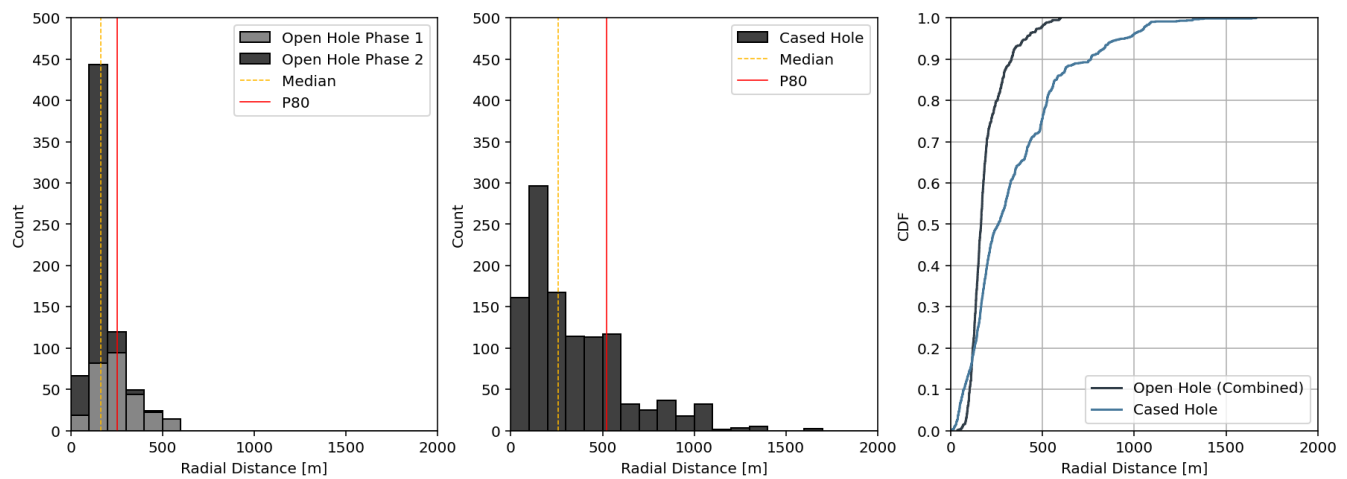


Figure 2-10: Distribution of Distance of Induced Events from Active Well for Open Hole (left) and Cased Hole (centre) Stimulation and Plotted Together as a CDF Plot (right)

Table 1: Distance to Event Data for the 3 Induced Seismic Data Sets

| Data Set | Completion Type | Distribution Type | Mean Distance (m) | Std Deviation (m) |
|--------------|-----------------|-------------------|-------------------|-------------------|
| 2022–Phase 1 | Open hole | Log Normal | 366.1 | 413.5 |
| 2022–Phase 2 | Open hole | Log Normal | 258.0 | 139.4 |
| 2024 | Plug & Perf | Log Normal | 150.3 | 45.0 |

2.3.3 Magnitude Distribution 2022 & 2024

The distribution of event magnitudes is shown below in Figure 2-11. Whilst both the open hole and cased hole completions experienced the same maximum magnitude, the cased hole experienced a narrower range of magnitude response, albeit higher.

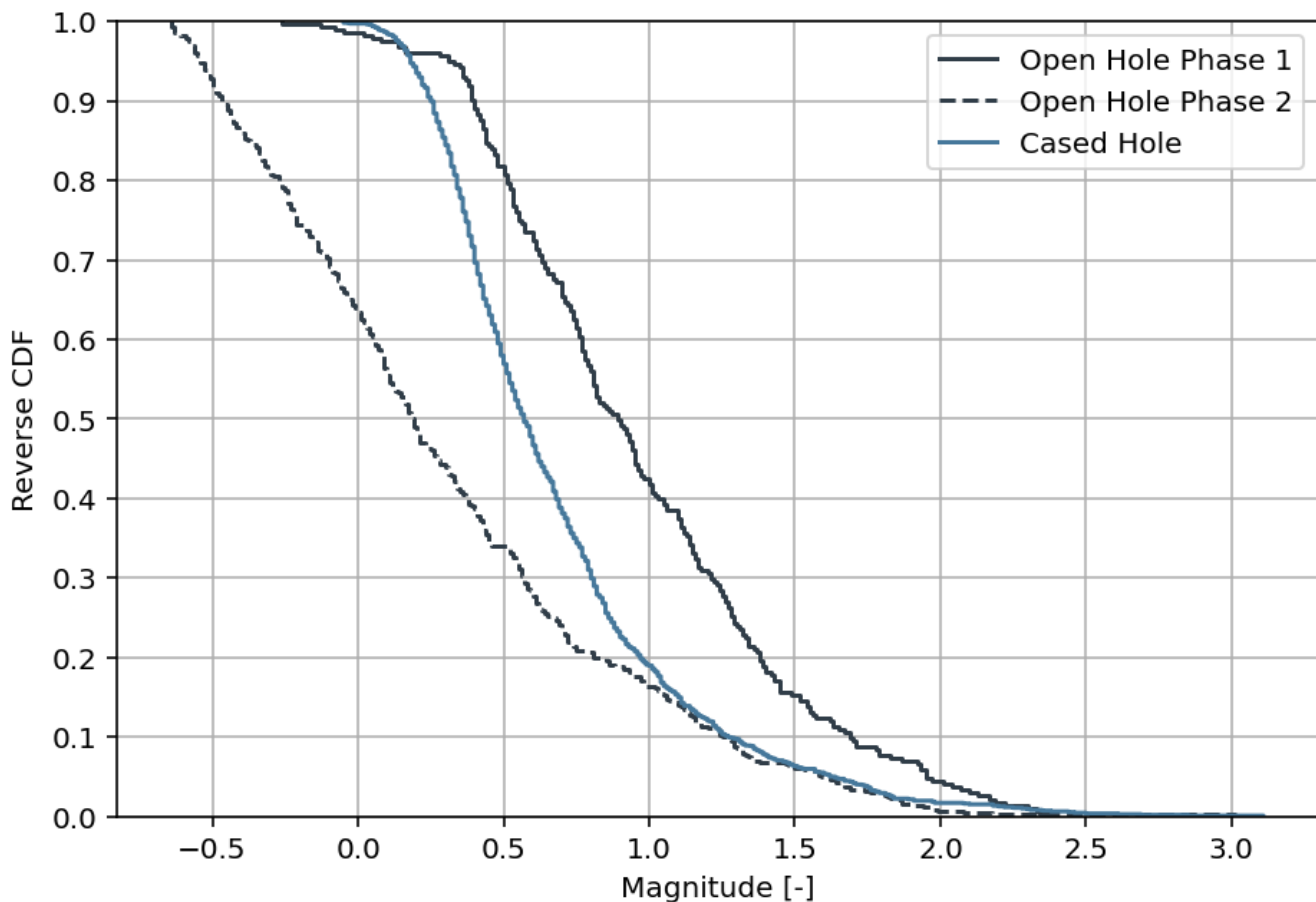


Figure 2-11: Distribution of Seismic Magnitude Response for the Open Hole (2022) and Cased Hole (2024) Completions

2.3.4 Data Set Comparison Summary

Analysis to date shows both similarities and differences between the two data sets:

- The distribution of magnitudes shows quite different patterns between the open hole and cased wells although they both show the same maximum magnitude. It is believed that the engineered “cased hole” completion results in a generally narrow range of magnitudes although the fault system itself strongly influences the maximum magnitude.
- The orientation of the induced lineaments for the 2022 dataset and 2024 dataset are within ~4 degrees (063 v 067 respectively), suggesting a very similar pattern of structures exist over a scale of >2 km, the distance between the two pads.
- The size distribution of induced lineaments from both datasets, all show a very similar trend, with a power law slope of -1. This also suggests a similar pattern of structures are being stimulated over this multi-pad scale.

- When the size distribution of the TGS seismic faults is added to the same power law plot, these faults have an almost identical gradient to the induced lineaments. Whilst there is some ambiguity about the normalisation area, it appears the intensity of the induced seismic lineaments is well aligned with the larger scale TGS seismic faults. We infer because of this power law relationship between the larger seismic structures and the smaller induced lineaments, that they are genetically related (i.e., the induced structures represent the smaller length range of the mapped seismic faults). This relationship has potential for pre-stimulation understanding of the fault system.
- The interpreted maximum horizontal stress orientation for the two pads shows some difference with 028 degrees for the 2022 dataset and 040 degrees for the 2024 dataset. The confidence in the 2022 SHmax direction is relatively low so it is considered that these two values are really very similar.

3.0 STOCHASTIC SIMULATION OF HYDRAULIC FRACTURE INDUCED SEISMICITY

3.1 DFN Model Description

DFN models are stochastic representations of subsurface structures, where the orientation, size and intensity of structures are drawn from distributions reflective of available characterization data (Rogers et al., 2010). We use the FracMan software (Golder, 2022) for DFN modelling and analysis. A truncated power law distribution (TPLD) is used to quantify the length of each fracture set. The TPLD is often used for DFN modelling because it reflects fracture size distributions observed in field studies (Davy, 1993; J.-R. de Dreuzy et al. 2002). The distribution of fractures under a TPLD is defined by a power law exponent (DI), minimum and maximum fracture lengths (l_{min} , l_{max}), and the volumetric fracture intensity (P32). We fix DI using observed lineaments, thus P32 and l_{min} become the primary driver of DFN connectivity. P32 is scale and orientation independent and inversely correlated with l_{min} (Dershowitz and Herda, 1992). We also correct P32 for fracture truncation which increases l_{min} and P32 collinearity. This collinearity is important in both DFN modelling and statistical inference. A supplement provides additional details on the TPLD and illustrates how P32 and l_{min} affect fracture connectivity.

The fractures are generated with dips of 90 degrees and extend beyond the region of interest in each model. Hydraulic fracture dimensions are informed by operator numerical modelling (Tan et al., 2022), microseismic observations (Maxwell et al., 2009), and fracture driven interactions (Gupta et al. 2021). HF orientations are deterministically assumed, based on the maximum principal horizontal stress (σ_H) direction. Once natural and hydraulic fracture sets are generated (Figure 3-1a), fractures that are directly or indirectly connected to the injection stages are identified (Figure 3-1b). Of the connected fractures, potentially seismogenic fractures are isolated. Seismogenic fractures are oriented oblique to σ_H , experience high shear stress (τ), and low normal stress (σ_n), and are thus prone to shear slip and seismic event generation (Figure 3-1c).

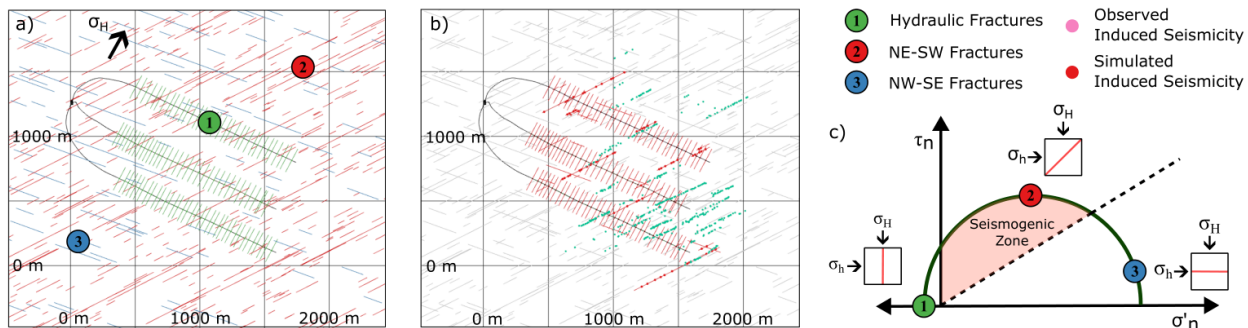


Figure 3-1: (b) Connected fractures (red) with Simulated (red) and Observed (green) Induced Seismicity. (C) Mohr's Circle Illustrating Fault Orientations that are Prone to Seismicity due to an Oblique Orientation to σ_H .

The Three Fracture Sets are Annotated along with Diagrams of Failure Modes for the Tension, Seismogenic, and Aseismic Regions of the Mohr's Circle

3.2 Fault Network Optimisation

Previous analysis attempted to find a match between the modelled fault network and induced seismic lineaments, primarily by changing the overall fault intensity. This time a number of parameters have been adjusted for each fault set by solving an inverse problem using the Levenberg-Marquardt (LM) algorithm (Levenberg, 1944, Marquardt, 1963). The LM algorithm iteratively minimizes the regularized objective function (Eq. 2) and perturbs a parameter vector (\mathbf{p}) via a sensitivity matrix (\mathbf{X}) and a diagonal weighting matrix (\mathbf{W}). The inversion is regularized by a dampening coefficient, or Marquardt lambda (λ). In the equation, \mathbf{I} is the identity matrix, \mathbf{y} is the observation vector, and $\bar{\mathbf{y}}$ is the estimation vector for each iteration k .

$$\mathbf{p}^{k+1} = \mathbf{p}^k + (\mathbf{X}^{Tk} \mathbf{W} \mathbf{X}^k + \lambda^k \mathbf{I})^{-1} \mathbf{X}^{Tk} \mathbf{W} (\mathbf{y} - \bar{\mathbf{y}}^k) \quad \text{Eq1}$$

The LM algorithm is implemented in the PEST software (Doherty, 2010), which uses FracMan as the forward model. PEST perturbs the model parameters proportional to their sensitivity (\mathbf{X}). The optimization parameters, initial values, parameter bounds, and observations are specified in a control file. FracMan outputs are evaluated automatically through postprocessed output files. The mean statistics of 25 DFN realizations are used to evaluate each iteration to minimize the impact of stochastic spatial variations. Realizations are generated using the current iteration parameters (P32, l_{mini} , hydraulic fracture length) but with different random seeds, thus generating a different discrete fracture network each realization. The objective function is made of several observations: the number and total fracture length of seismogenic lineaments and the distance between simulated seismic events and the nearest HF stage. The inference attempts to reproduce the distance distribution by using seven quantiles corresponding to the median and +/- 1, 2, and 3 standard deviations, assuming a normal distribution. The distance bins are also used to represent the number of events at various distances from the HF stages.

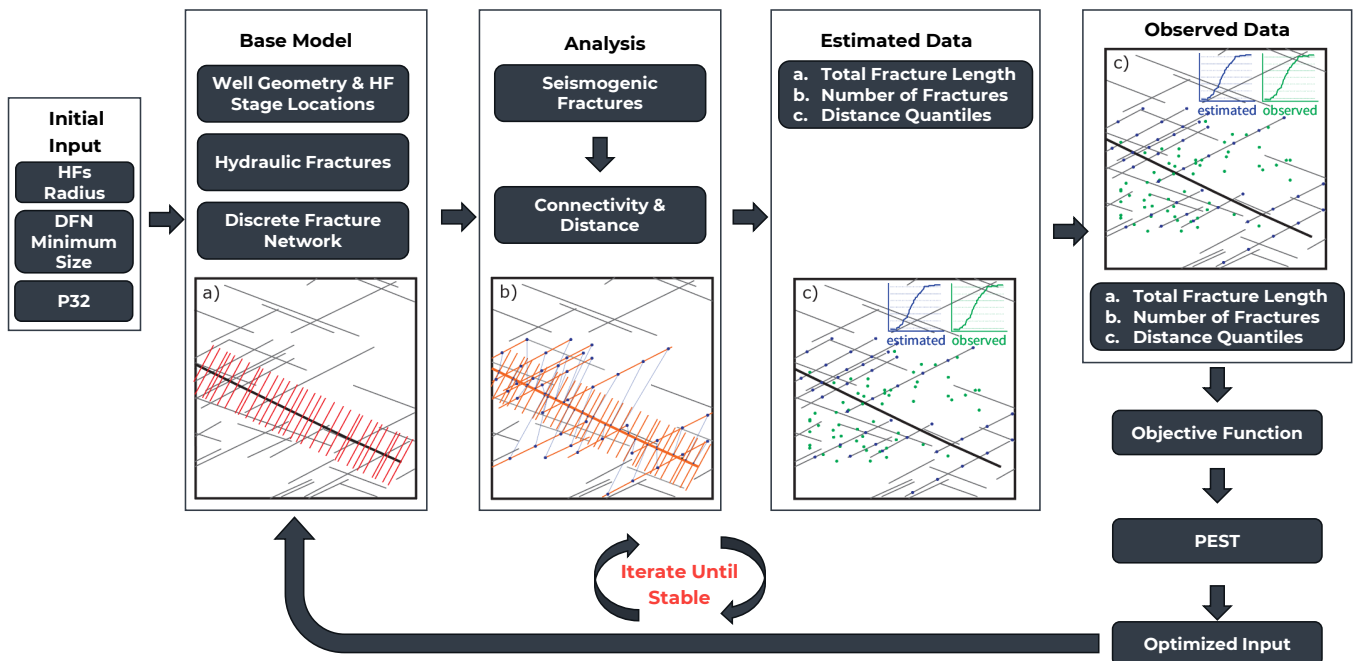


Figure 3-2: The PEST Workflow for Estimating the Best DFN Model

The G16 dataset was used in building a Base Model, consisting of the existing well, and Hydro-Fractures (HFs) stage locations. A DFN is simulated around the Base Model, consisting of:

- two fracture sets – Set A (trending NE-SW) and Set B (trending NW-SE). The first two input parameters for optimization are the P32 and Minimum Radius Size for both sets
- HFs are generated by assigning a constant size distribution value, governed by the last input parameter for optimization – **HF Radius**

“Seismogenic” fractures from **Set A** that connect either directly or indirectly to the HFs are then isolated and used to estimate fracture characteristics and distance between simulated events and the nearest HF stage. The result is an **Estimation Dataset** –

- Total length of all seismogenic fractures
- Total number of seismogenic fractures
- Distance quantiles

The **Estimation Dataset** is compared against the **Observations Dataset** (actual microseismic or induced events data), with the comparison being used to update the LM objective function using **PEST** for the input parameters in the next iteration. This process is repeated until a stable inference is obtained. That is a good match between the observed and simulated properties in question.

The input ranges and best matched properties are summarised in Table 2.

Table 2: Summary of Key Input Parameters, Ranges and Optimised Estimate from 2022 and 2024

| Name | Initial Value | Bounds | | 2024 Estimated | 95% Percent Confidence Limits | | 2022 Estimates |
|------------------------|---------------|--------|-------|----------------|-------------------------------|--------|----------------|
| | | Lower | Upper | | Lower | Upper | |
| Set A P32 | 0.005 | 0.0001 | 0.01 | 0.0013 | -0.001 | 0.004 | 0.0031 |
| Set B P32 | 0.005 | 0.0001 | 0.01 | 0.0096 | 0.003 | 0.017 | 0.0014 |
| Set A – Min Size | 100.00 | 25.0 | 499.0 | 95.5 | 24.3 | 166.7 | 45 |
| Set B – Min Size | 100.00 | 25.0 | 499.0 | 145.6 | -1083.4 | 1374.7 | 90 |
| Hydraulic Fracs Length | 220.00 | 160.0 | 300.0 | 236.4 | -3116.2 | 3589.1 | - |

3.3 Selection of Best Matched Scenarios

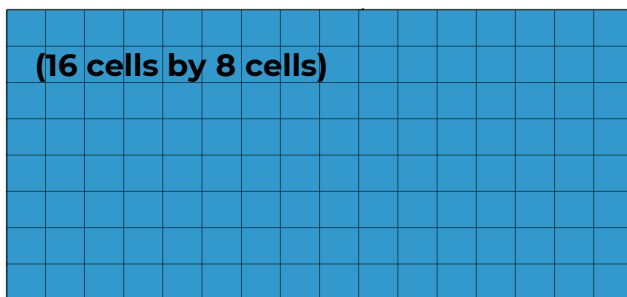
The PEST analysis selects the DFN model with the best global property match. To help select a model with a better overall spatial match as well, a screening workflow was developed to select the best realisation out of 10,000 that matched the observed data.

The following workflow was used to select the best fit realization:

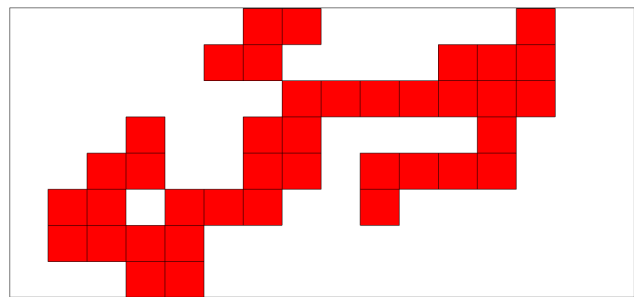
- Generate 10,000 realizations and build a grid with 200 m × 200 m cells to cover the modelled extend of each realization.
- A property is created and flagged whether an observed fault was present or not at that cell (0 (no) or 1 (yes)).

- A property is created and flagged whether a simulated fault was present or not at that cell (0 (no) or 1 (yes)).
- The two properties (observation data and simulated data) are combined by multiplying the two grids together resulting in either a 0 or 1. Where an observed and simulated fault are coincident in the same cell, a score of 1 is achieved. Where they are not coincident, the score is zero.
- By summing the value of all cells in the combined property, a best of fit score is calculated as a measure of the spatial goodness of the simulated faults relative to the observed faults, Figure 3-3.

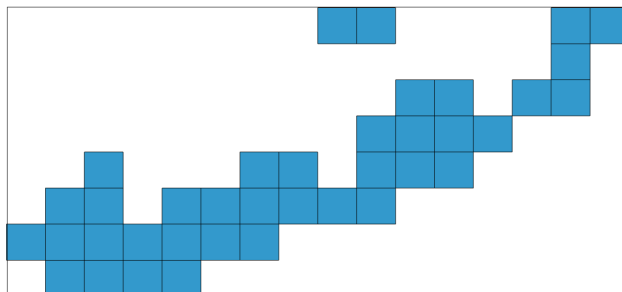
a) 200m x 200m grid



c) Simulated fault location



b) Observed Fault Locations



d) Obs * Sim properties

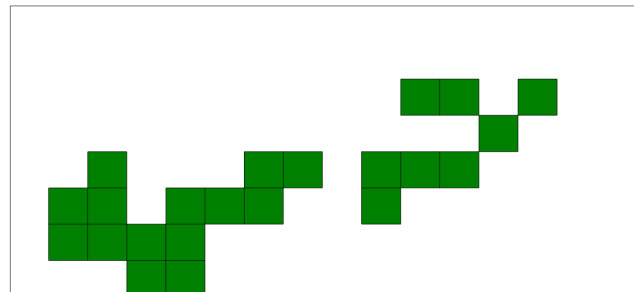


Figure 3-3: Workflow for Selecting Optimum PEST Realisation. a) 250 × 250 m Grid, b) Observed Faults Mapped into the grid, c) Simulated Faults (One Realisation) Mapped into the Grid, and d) Product of Two Grids where Observed and Simulated Agree

Following the scoring process, the list of realizations is further filtered to improve the matched realisations.

- The observed number of realisations was 20 so only realisations with between 18 to 22 (10% of 20 observations) were selected.
- The total observed length of lineaments was 5,157 m and so only realisations between 4,900 m to 5,415 m (5% of 5,157 m observation) were selected.

The top six (6) fitting realizations were picked and subsequently manually reviewed with two (2) realizations being selected for the subsequent 3DEC numerical analysis, Figure 3-4.

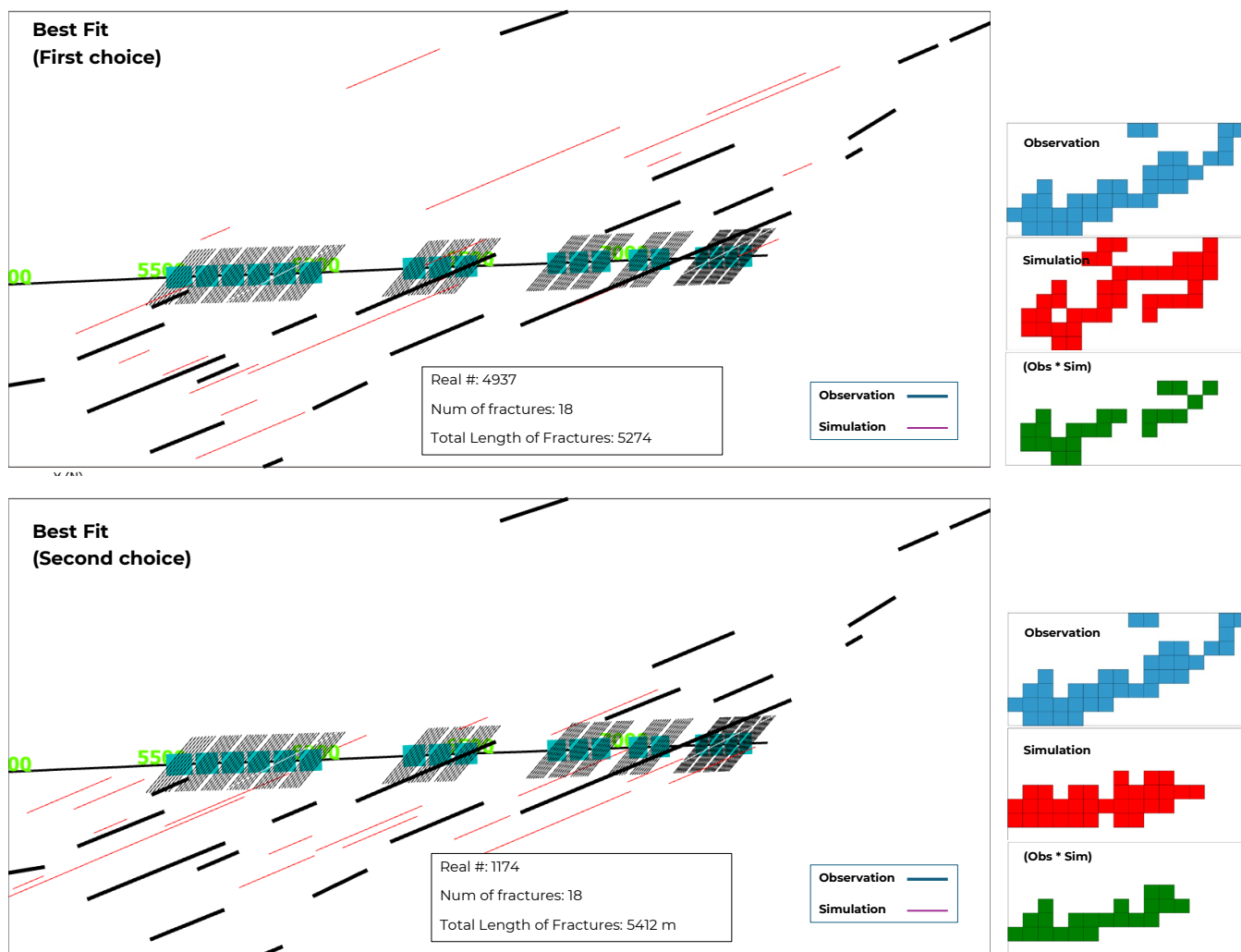


Figure 3-4: Best Two Realizations Selected for the 3DEC Numerical Analysis

3.4 Stochastic Simulation Summary

A DFN description of the 2024 pad has been built which shows that the overall fault geometry is similar to the 2022 pad despite being >2 km away. We have run the PEST analysis in an attempt to optimise a number of parameters of this network using automatically, rather than the previously attempted brute force manual method. The results show that the approach can be used to actively optimising a range of DFN input properties in an objective way, removing the subjectivity of the manual calibration. The raster based selection method (Section 3.3) has proved to be an effective way of selected the best quality matches from a large number of realisations (N=1000). However, it also highlights the probability of generating a precise match that honours the spatial intensity, distance from wells, and overall connectivity is low when using a single Poisson process modelling step.

3.5 Using the DFN Model to Evaluate the Impact of Frac Length

The DFN model has been used to explore the impact of completion style on likely induced seismicity. A key difference between plug and perf and open hole completions is often the length of the hydraulic fractures, with open hole created hydraulic fractures typically extending further than plug and perf created ones. A base case modelling scenario using hydraulic fractures with a half length of 75 m (total length 150 m), consistent with shorter plug and perf completions, was compared against a model with longer hydraulic fractures with a half length of 300 m (total length 600 m), consistent with open hole completions. In addition a comparison between having 600 m long hydraulic fractures at closely spaced perfs and also a single long frac for each stage. No notable difference was seen between these two long frac scenarios and so only the models with multiple frags per stage have been reported, Figure 3-5.

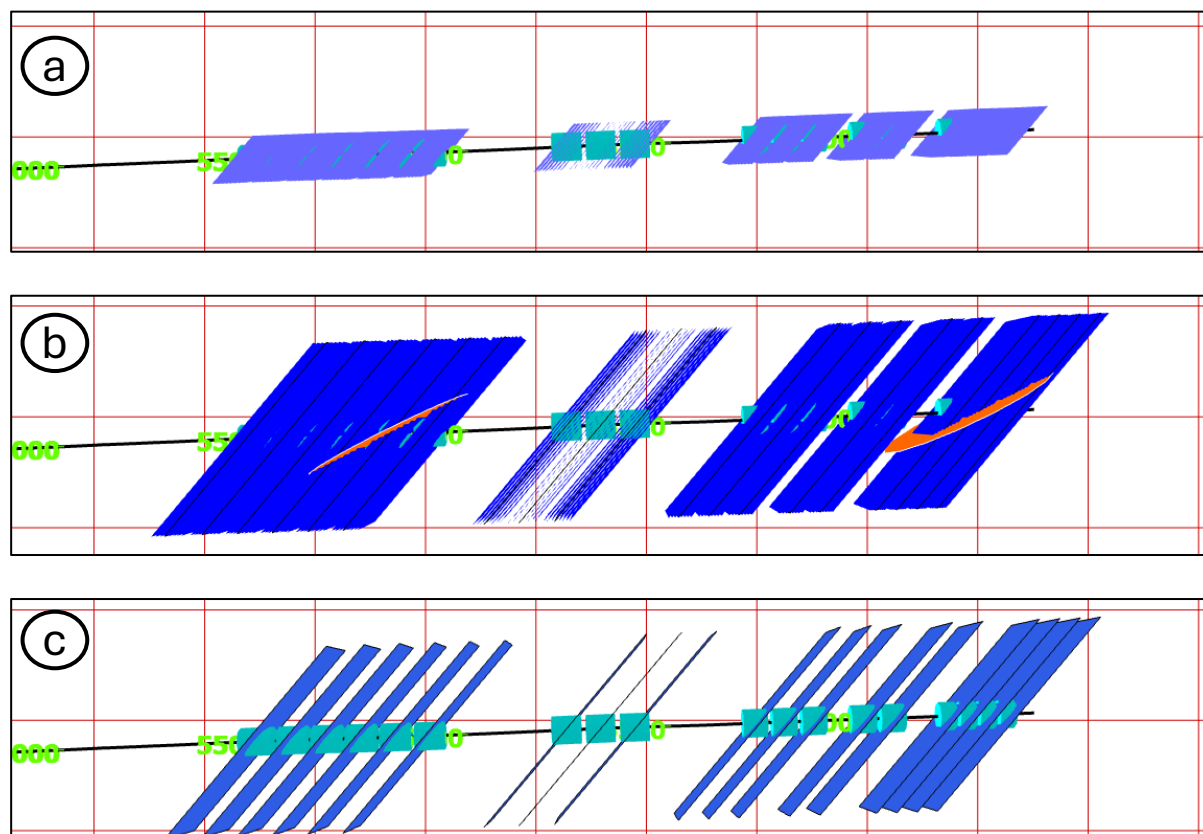


Figure 3-5: Simulated Hydraulic Fracture Length. a) 150 m Full Length Hydraulic Fractures at Perf Centres, b) 600 m Full Length Hydraulic Fractures at Perf Centres, and c) 600 m Full Length Hydraulic Fractures, One Frac Per Stage

Using the optimised DFN properties, 50 realisations of each model were generated, with the total connected fracture population being identified for the two scenarios. These results have been compiled in a number of ways:

- As heat maps of connected fractures around the wells for the two scenarios.
- As CDFs of the distance of structures from the active stages for the two scenarios, and
- As CDFs of the distribution of both connected area for the two scenarios.

The DFN modelling is a stochastic process, generating multi-equiprobably realisations of the likely connected structures. Examples of the likely connected structures from the 150 m long hydraulic fractures and 600 m fractures are shown in Figure 3-6 and Figure 3-7, respectively. These connected fractures represent the maximum effective stimulated volume than could be reached. Note that there is similarity between the cases in the two scenarios. This is because the models are generated with the same random seed number, so both iteration 1 models (for the 150 m and 600 m models) share the same underlying DFN model, and the impact of the different hydraulic fracture length is the primary driver on the difference between the results. It is clear to see that the 600 m frac models result in a larger stimulated volume than the 150 m frac models.

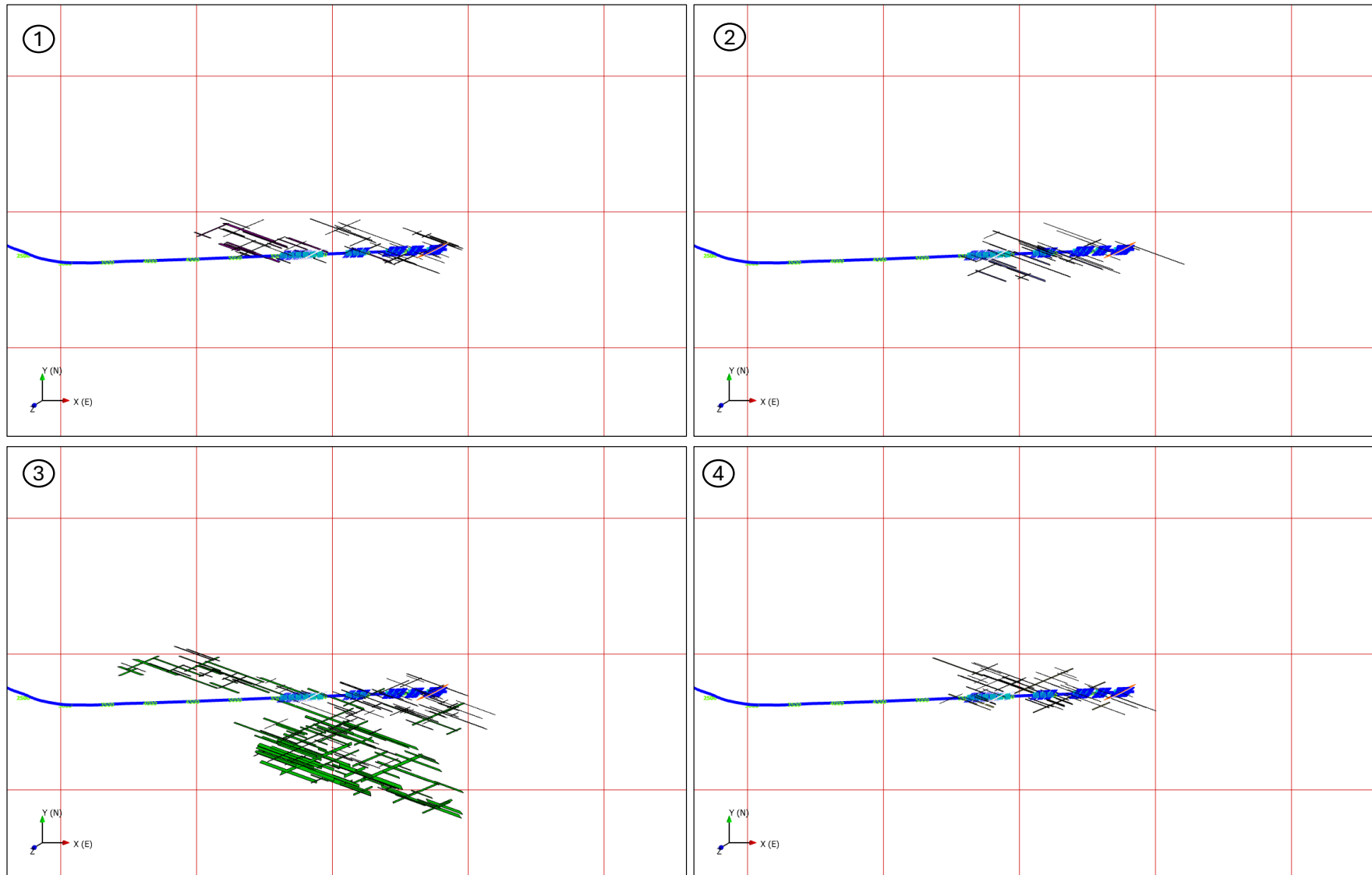


Figure 3-6: Realisations 1-4 (or 5) Showing the Connected Fractures (Stimulated Volume) for 150 m Long Hydraulic Fractures. Grid Squares are 2000 × 2000 m

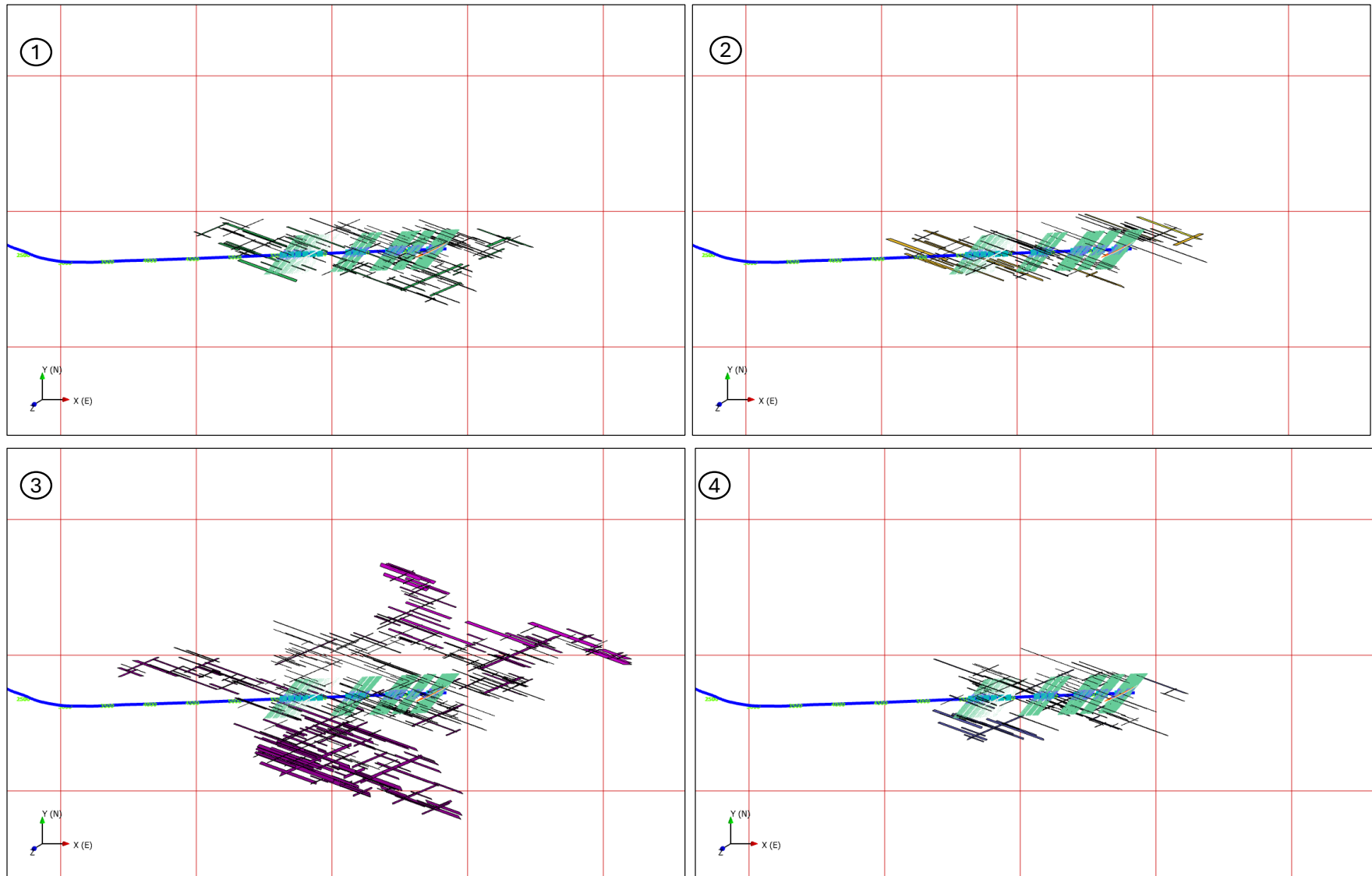


Figure 3-7: Realisations 1-4 (or 5) Showing the Connected Fractures (Stimulated Volume) for 600 m Long Hydraulic Fractures. Grid Squares are 2000 × 2000 m

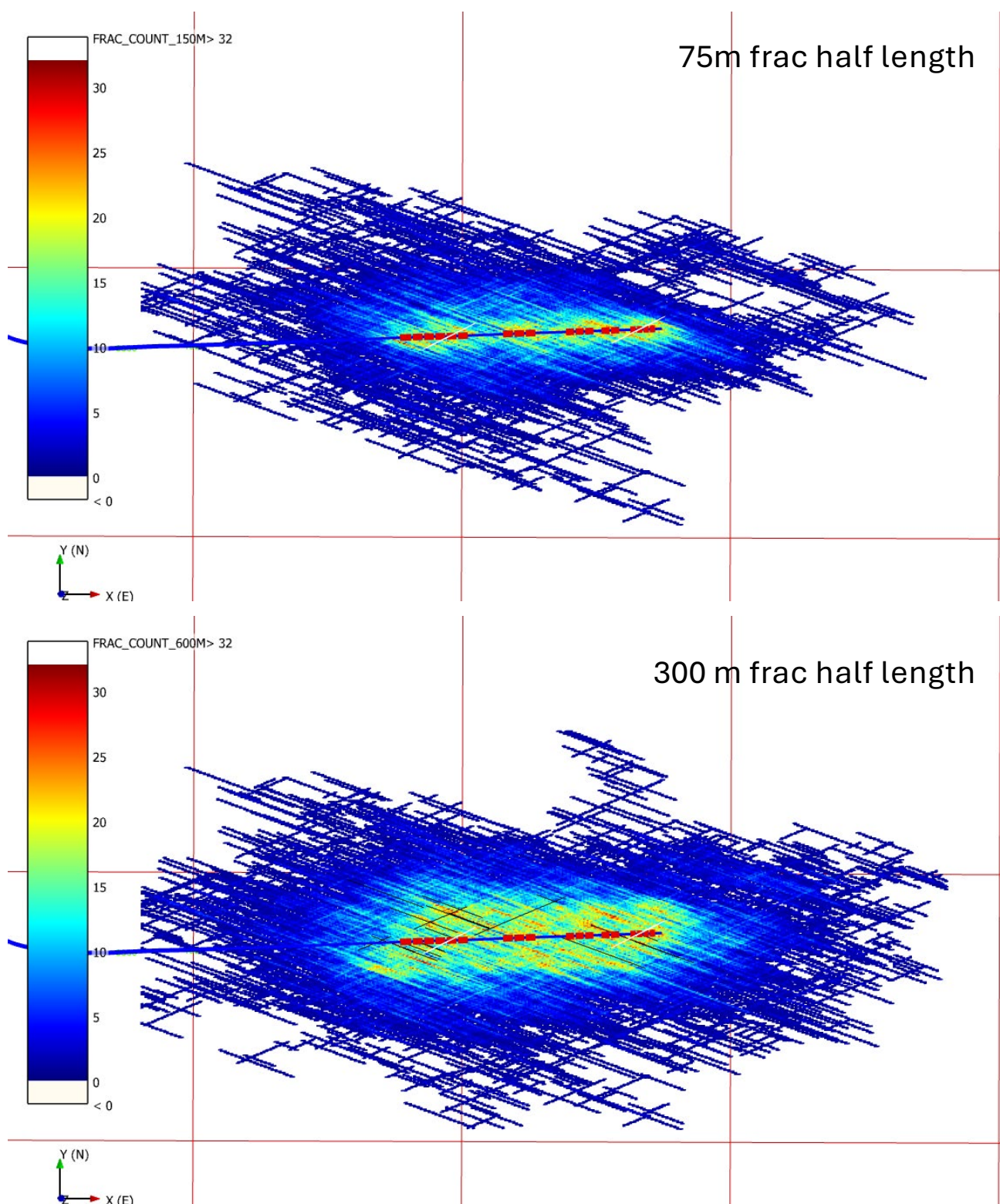


Figure 3-8: Density Plot of Fracture Count from Compiling 50 Realisations of the Connected Fracture Results for Top) 150 m Long Hydraulic Fractures, and 600 m Long Hydraulic Fractures. Red Grid Cells are 2000 × 2000 m

To help visualise the 50 realisations that were generated for each model, heat maps were generated by flagging all cells in a fine grid (1×1 m cells) constructed over the modelling volume for each realisation. The heat maps therefore show how many realisations occur at a particular location (zero = no realisation occurs at that location, 50 = fractures are there in all realisations). The heat maps shown in Figure 3-8, show the density of the 50 realisations for the models with the 150 m long hydraulic fracs (top) and the 600 m long fracs (lower). What these heat maps show is that whilst the overall area covered by the 600 m frac model is slightly larger than the 150 m frac model, really it is the area closer to the well where there appears to be the greatest distance. Note how the degree of connectivity within the first 500 m is far greater for the longer frac model.

To illustrate this further, the distribution of distance from active stages to all connected fractures has been plotted for both models, Figure 3-9. On the left and centre are histograms of this distance for the 150 m and 600 m models respectively. ON the right are CDFs of the two models. The CDFs show that the 600 m frac model extends approximately 75 m further than the 150 m model, with a peak distance 2150 m compared to the shorted frac model, with a peak distance of 1900 m. The histograms also show the 80th percentile (P80) distance for the two models with the 150 m model having a P80 of 500 m, compared to a P80 distance for the 600 m model of 600 m.

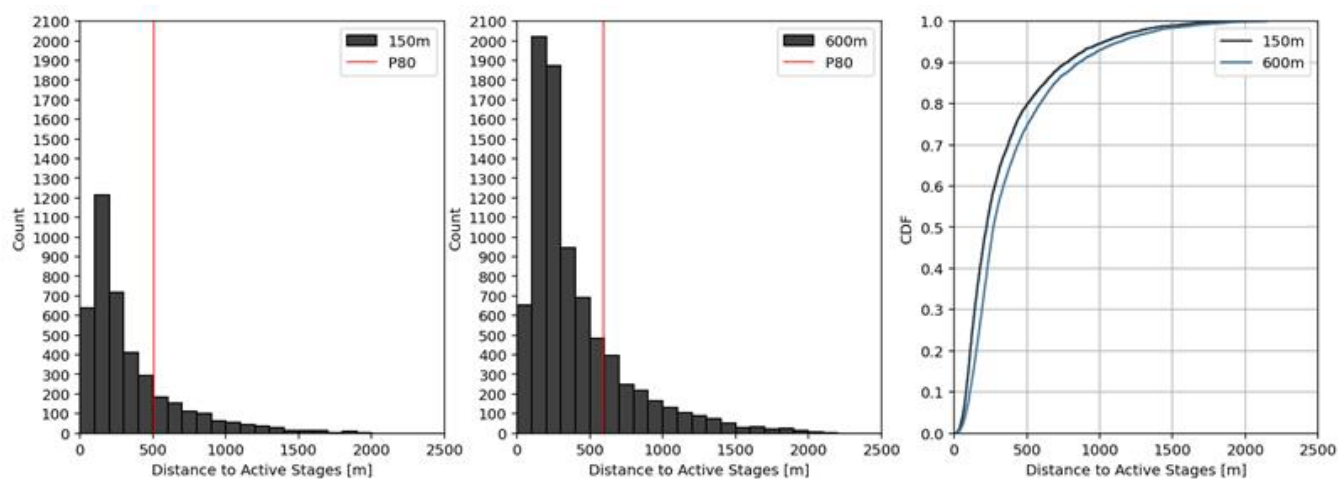


Figure 3-9: Distribution of the Distance from Active Stages to Connected Fractures. Left) 150 m Frac Lengths, Centre) 600 m Frac Length and Right) Cumulative Frequency Distribution (CDF) for the 2 Models

The results in Figure 3-9 confirm the observations from the heat maps in Figure 3-8, that the overall connected distance from active stages into the reservoir is slightly greater for the longer fracs considered more representative of open hole completions than the shorter plug and perf completion type fracs. The models were further explored to examine both the total number of fractures indirectly connected to the active stages and also the total connected fracture area. CDFs of these two properties are plotted in Figure 3-10. These CDFs show that for both parameters there is approximately a 2 fold increase in the number of connected fractures and connected fracture area for the longer (600 m) fracs. This is quite an increase in connected area, given the at best 15-20% increase in connected distance. It is worth pointing out that this connected fracture area has the potential to provide an enhanced production profile, with the potential for considerable natural stimulated area to provide production.

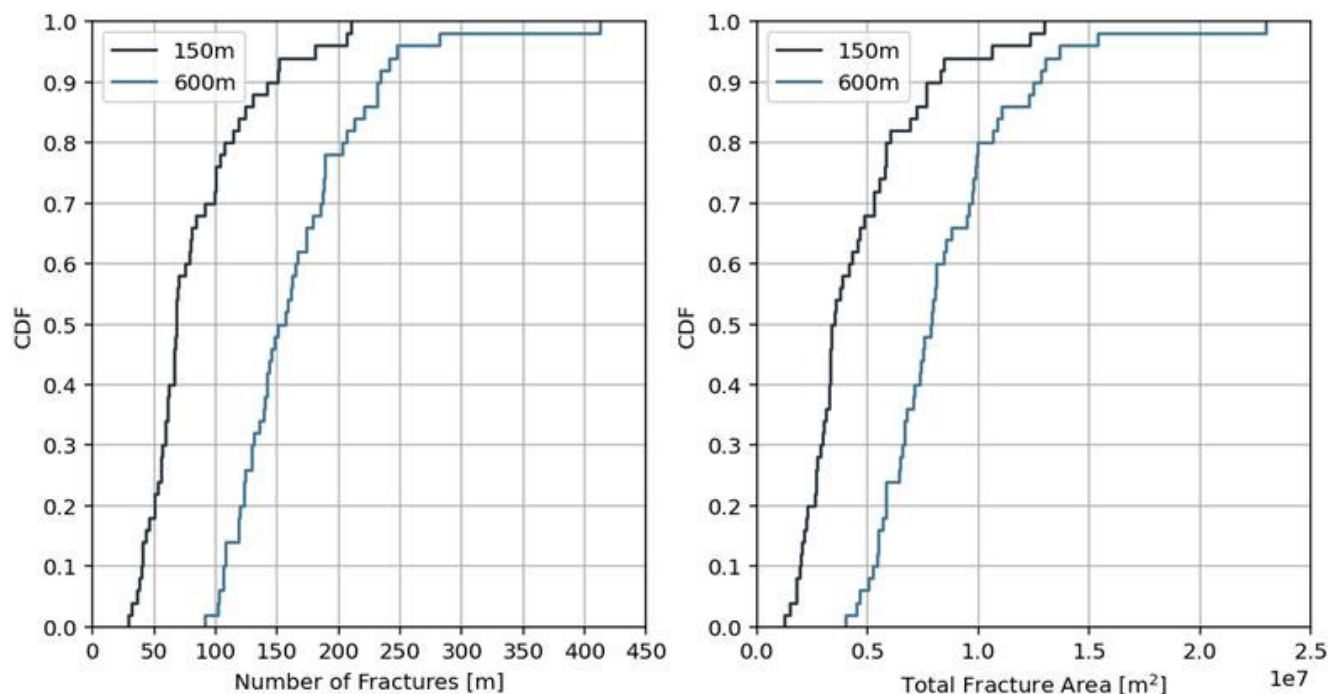


Figure 3-10: (Left CDF of Connected Fracture Count for the 150 m and 600 m Frac Models; and left) CDF of Connected Fracture Area for the 150 m and 600 m Frac Models

3.6 DFN Summary

The DFN analysis describes how the reservoir fault fabric has been inferred and optimised by reproducing induced seismicity through the identification of connected NE-SW seismogenic structures and inferred NW-SE aseismogenic faults. The basic conceptual model has been shown to reproduce the broad spatial pattern of events including the distribution of the distance of the events from the well. In contrast to previous work, this this optimised matching has been achieved using the PEST code (Parameter Estimation). The results from the 2024 data set are very similar to 2022 analysis where a more manual matching process was achieved for the data set to the north.

Using the DFN model to investigate changes in the connected population as a function of hydraulic fracture length. These results showed that the longer (open hole) fracs result in potential seismicity extending a little further away from the well (P80 distance for 150 m fracs 500 m, and 600 m for 600 m fracs). However, the longer fracs do result in the increased connection to reservoir fractures (both count and total area) and it is believed that this does increase the seismic potential of open hole stimulation relative to shorted plug and perf fracs.

4.0 NUMERICAL SIMULATION OF HYDRAULIC FRACTURE INDUCED SEISMICITY

4.1 Introduction

The previous section of the report detailed the DFN based analysis and optimisation of the inferred structural fault fabric within the Lower Montney unit, using a simple geomechanics scheme as follows:

- Aligned induced seismic (NE-SW orientated) events indicate the presence of a seismogenic population of faults, that are connected either directly or indirectly to the hydraulic fractures at the well.
- Additionally, there are inferred aseismogenic structures (NW-SE orientated) that whilst seismically invisible, do allow the diffusion of pressure out through the wider network.
- Pressure perturbation from injection through the hydraulic fractures and subsequent connected network of seismogenic and aseismogenic structures, results in the generation of induced seismic events.

The DFN analysis represents a purely geometrical solution to the investigation of induced seismicity. Whilst being a sound geomechanical hypothesis, it is not a physics based simulation that can explore critical controls on the response of the reservoir to injection and the resulting induced seismicity. To achieve this, the optimised DFN model has been converted to a numerical geomechanical simulation, allowing the simulation of hydro-mechanical processes. That is, pressurised fluid is injected into the hydraulic fractures and moves into the connected fault network, with the apertures of the fracs and faults responding to this injected fluid and within the geomechanical earth model defined by the in situ stresses and stiffnesses of the reservoir. These coupled models are slow to run in comparison to simple flow models, with coupled simulation times taking days, in comparison to minutes for uncouple models. As a consequence of the computational cost of these coupled models, some simplifying assumptions have been described within this section. The objectives of these simulations have been to inject pressurised fluid into the discrete fracture model with a view to achieve the following:

- Validate the overall conceptual geomechanical model as described above, including:
 - The generation of seismicity of broadly the same magnitudes, occurring on the NE-SW orientated structures, broadly to the extent of the connected fracture zones included with the model.
 - The diffusion of pressure along both NE-SW and NW-SE structures with limited to no seismicity occurring along the NW-SW structures.
- Investigate the potential mitigation of seismicity through operational controls such as injection rate, ramp up rate and fluid viscosity.
- To compare the impact of shorter length limited entry, plug and perf hydraulic fractures versus longer open hole hydraulic fractures on seismicity generation.

4.2 Model Construction

The first step of the numerical model construction is to extract the optimised DFN model. The best matched model was extracted and the hydraulic fractures simplified from one frac per perf to one frac per stage, see Figure 4-1.

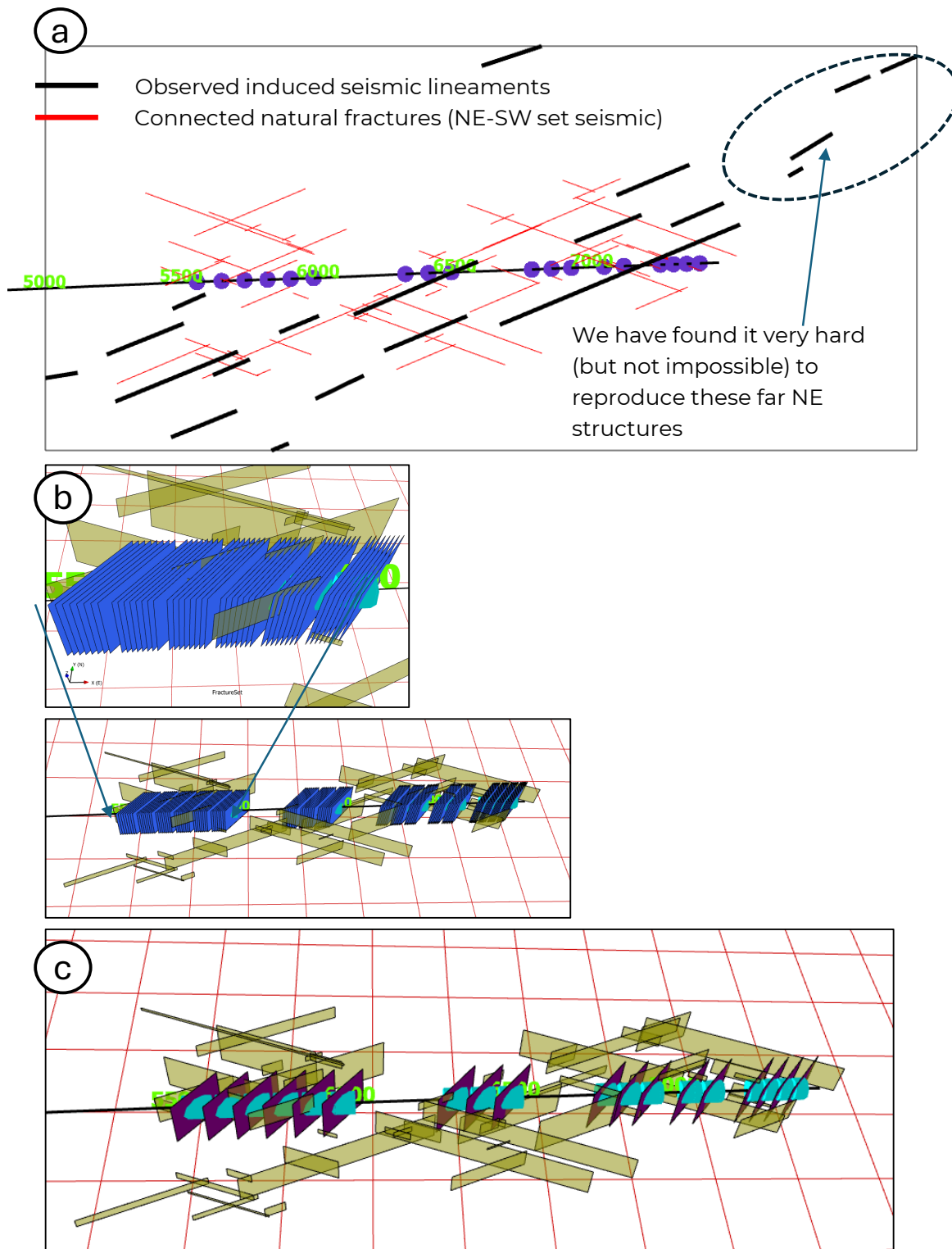


Figure 4-1: Development of DFN Derived Structural Model into 3DEC Ready Model. a) Red Lines Represent the Best Matched Connected Fault Network. b) Original Hydraulic Fractures in DFN Analysis used Tightly Spaced Fracs for Each Perf. c) The Final Model Replaces the Perf Clusters with Single Frac Per Stage to make the Analysis Simpler

To build the geometry, the DFN model of faults and hydraulic fractures shown in Figure , was imported into 3DEC version 7.0 (Itasca 2025). 3DEC is a numerical modelling software developed by Itasca for simulating the mechanical behavior of fractured rock masses using a distinct element approach. It represents the rock mass as discrete blocks separated by joints or faults, making it ideal for analyzing structurally complex ground conditions. When combined with a Discrete Fracture Network (DFN), which statistically characterizes fracture systems, 3DEC can perform coupled hydro-mechanical modelling to evaluate how fluid flow through fractures interacts with the stress and deformation in the rock mass.

To optimize the geometry, a smaller scale block was developed around the main connected faults and hydraulic fractures, within which a finer mesh was generated (Figure 4-2). This approach improves model efficiency by optimizing run time and enhancing result accuracy.

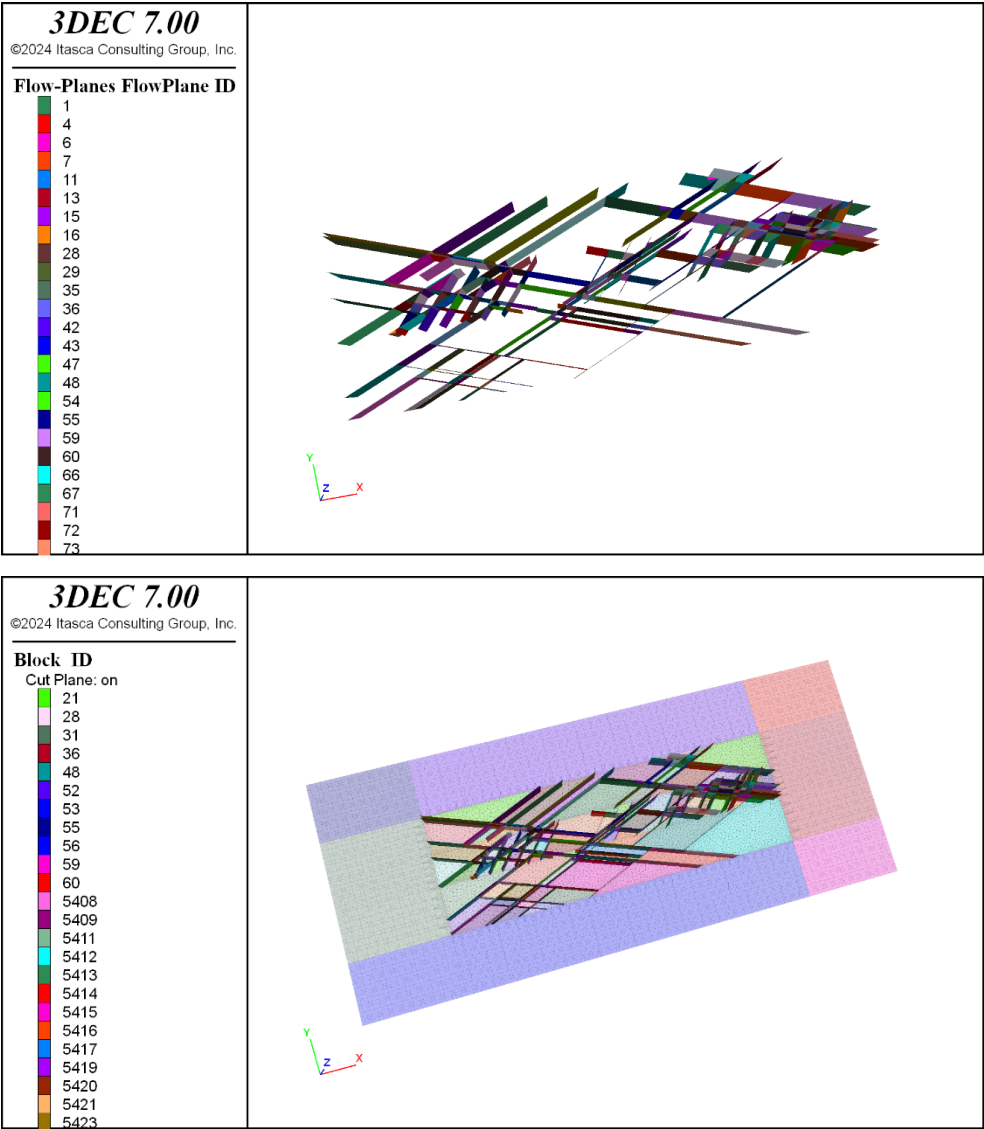


Figure 4-2: Conversion of the DFN Model into a 3DEC Model. Upper Image shows the Connected Fractures (Both Hydraulic Fracs and Faults), and the Lower Image shows the Completed Model Imbedded within the 3DEC Model

4.3 Model Parametrisation

The constructed 3DEC model represents the Lower Montney layer, with thickness of 150 m (from logs). Some of the larger structures extend along the Montney layer from top to bottom of the unit, while others only extending a small height (e.g., the hydraulic fractures). The average injection depth is set to -2355 m. The main parameters used in the model are summarised in Table 3, Table 4 and Table 5. Note that, fluid stiffness has been optimized to improve the computational time.

Table 3: Summary of In Situ Stress

| In Situ Stress | Equations | Orientation | Source |
|------------------------|-----------------------|-------------|---------------|
| σ_H (MPa) | $1.3 \times \sigma_h$ | 0/040 | Assumed ratio |
| σ_h (MPa) | 25 Kpa/m | 0/130 | DFIT data |
| σ_v (MPa) | 0.026× depth | Vertical | Measurement |
| Pore pressure gradient | 14.2 Kpa/m | - | DFIT data |

Table 4: Summary of Rock and Fluid Properties

| Property | Values | Source |
|-------------------------|---------------------------|-------------------|
| Fluid Properties | | |
| Fluid density | 1447.50 kg/m ³ | Estimated |
| Fluid bulk Modulus | 3 MPa | Estimated |
| Fluid compressibility | 0.3 MPa | Estimated |
| Fluid dynamic viscosity | 0.002 Pa.s = 2 cp | Estimated |
| Rock Properties | | |
| Average Rock Density | 2600 Kg/m ³ | Estimated |
| Average Young's modulus | 57.4 GPa | From elastic logs |
| Average Shear Modulus | 21 GPa | From elastic logs |
| Average Poisson's ratio | 0.213 | From elastic logs |

Table 5: Summary of Joint Mechanical and Hydraulic Properties

| Property | Values | Source |
|------------------------------------|----------------------|------------|
| Joint Mechanical Properties | | |
| Normal Stiffness | 50 GPa/m | Assumption |
| Shear Stiffness | 50 GPa/m | Assumption |
| Friction Angle | 20 deg | Assumption |
| Cohesion | 0 Kpa | Assumption |
| Tension | 0 MPa | Assumption |
| Joint Hydraulic Properties | | |
| Residual Hydraulic Aperture | 1×10^{-4} m | Assumption |
| Aperture at zero normal stress | 5×10^{-4} m | Assumption |

Injection into the model is based around a single point at the well, with fluid injected into the centre of the hydraulic fracture and outwards into the wider fault network. The fracs are premade and there is no attempt to grow them as that would make the modelling highly challenging. The objective is to look at fluid and pressure movement through the fault network rather than frac growth. Using premade fracs reduces modelling time and complexity considerably. The pumping scheme for each stage is summarised below in Table 6.

Table 6: Fluid Pumping Scheme

| Property | Values | Source |
|--------------------|--------------------------|-----------------|
| Injection Pressure | 70.8 MPa | From field data |
| Injection Rate | 10.9 m ³ /min | From field data |
| Injection Volume | 443 m ³ ‡ | From field data |
| Injection Duration | 40.4 min‡ | From field data |

‡ – total volume and injection duration reduced to reduce model run times.

To reduce modelling time, a number of modifications to the actual stimulation sequence have been made:

- The overall injection period has been reduced from approximately 70 mins to 40 min with an associated reduction in total injected volume.
- There is no shut in time between stages as it is not believed that the model will accurately capture the relaxation post injection. The removal of this shut in period, reduces overall run times.
- The total number of injection stages has been reduced from 18 to 10, Figure 4-3. Many of the total stages stimulated similar structures and so a subset of stages was selected to capture the stimulation of the overall connected structure, whilst reducing the amount of modelling involved.

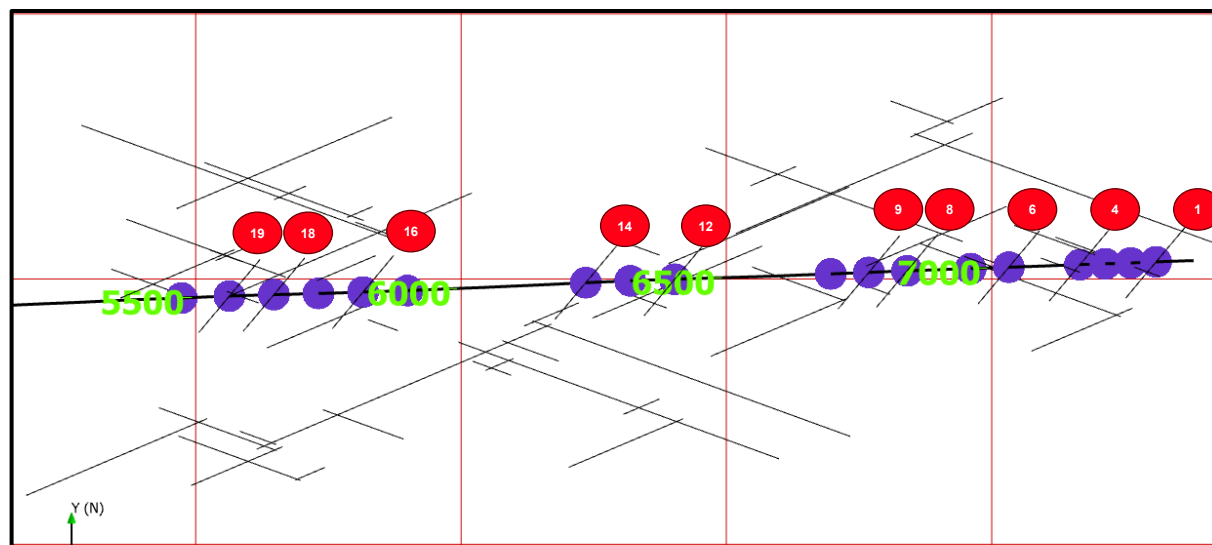
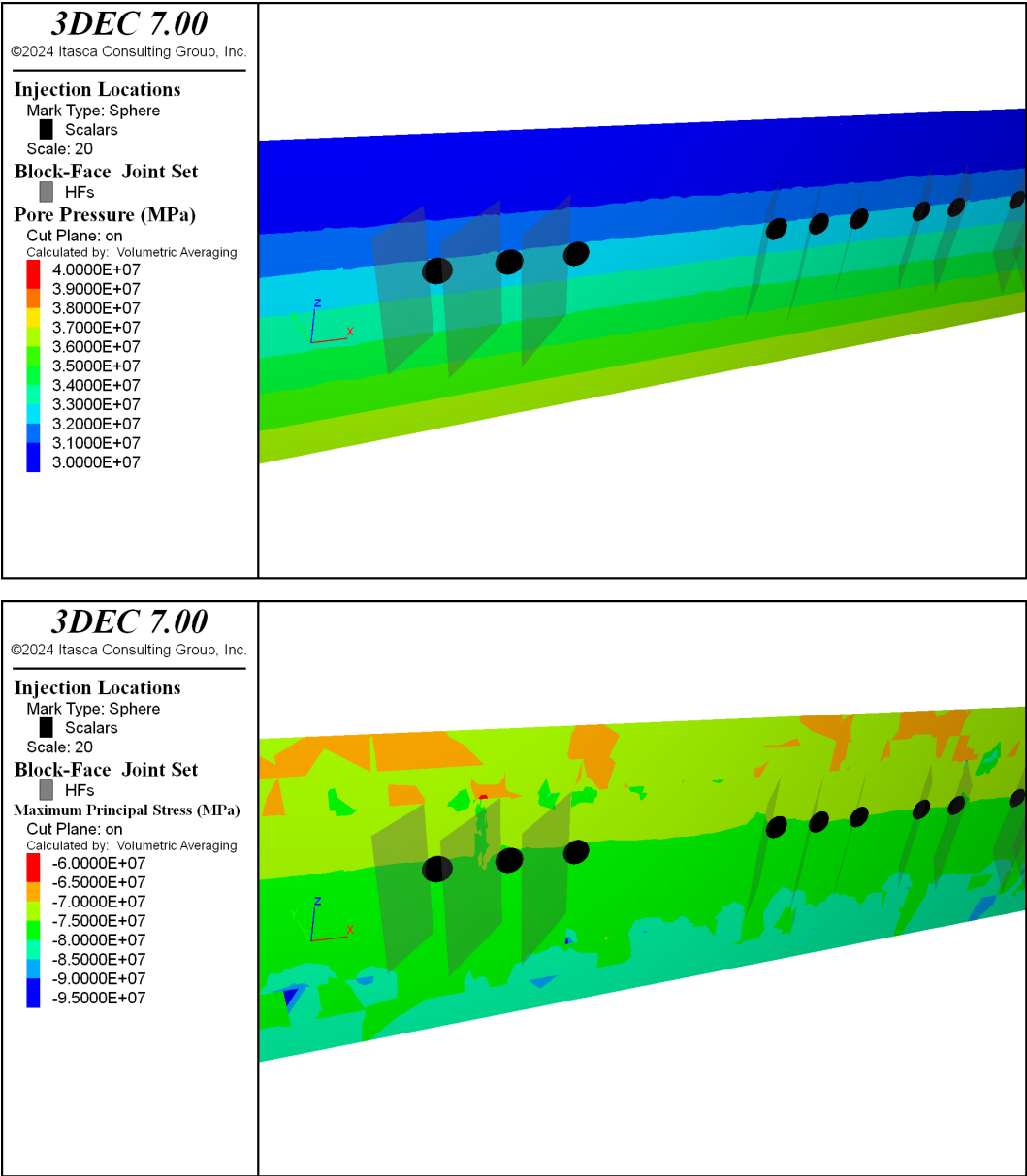


Figure 4-3: Modified Injection Stages to Reduce Simulation Time. 18 Original Stages (Purple) Reduced to 10 (Red)

4.4 Model Initialisation and Computation

The boundaries of the model are fixed laterally on vertical boundaries and the base in all directions and the surface is free. In situ stresses, pore-pressure and gravity has been applied as an initial state and then the model was cycled to reach equilibrium. In situ pore pressure, minimum and maximum principal stress contour plots are presented in Figure 4-4.



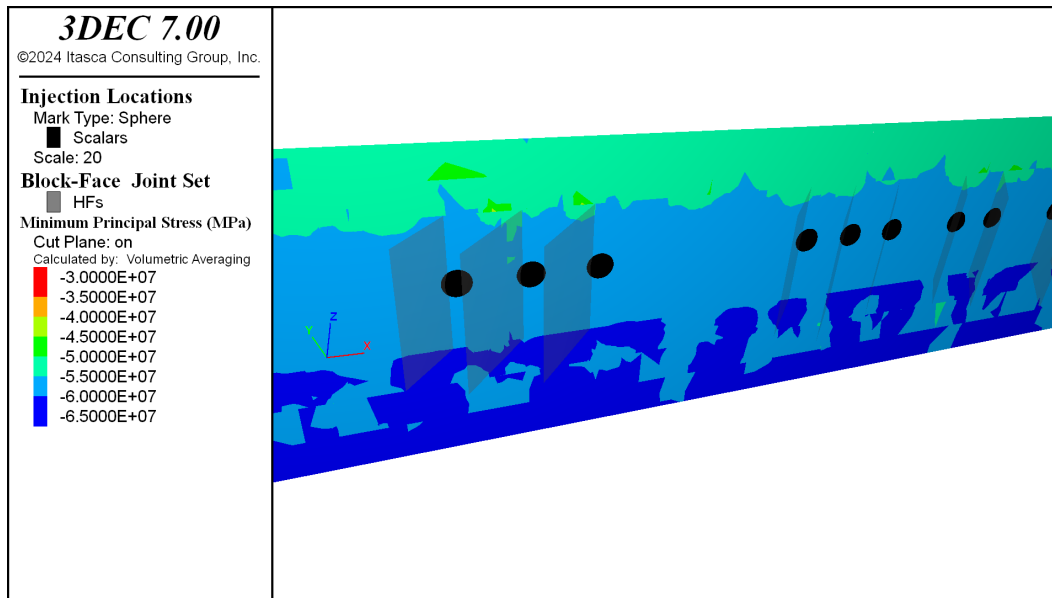


Figure 4-4: Contour Plots for In Situ Pore Pressure, Maximum and Minimum Principal Stress After Initial Equilibrium (before Fluid Injection)

Once the model was initialized, the fluid injection was simulated using the assumptions presented in Section 4.3. A sequential injection was defined for the ten selected stages. Multiple history points were identified at the location of injections to monitor pore pressure changes over time. Seismic moment, seismic moment magnitude and in return seismic energy were calculated after completion of each injection cycle for the contacts that have undergone shear displacement.

The Moment Magnitude (M_w) is a dimensionless number and the subscript “w” stands for mechanical work (Hanks and Kanamori 1979). A log scale is used, given as:

$$M_w = \frac{2}{3} \log M_0 - 6$$

Here, M_0 denotes seismic moment with dimensions of energy ($N \cdot m$) (Hanks and Kanamori 1979). Seismic moment (M_0) is the total strain energy released during an earthquake:

$$M_0 = \mu AD$$

Here, μ is the shear modulus of the faulted rock (shear stiffness of the joints in the current study), the A is the shear-stimulated area (area of the fault) and D is the average shear displacement on shear-stimulated area. Therefore M_0 has units of work ($W = F \cdot d = \mu \cdot A \cdot d$).

4.5 Model Results

The following plots were generated to interpret numerical results:

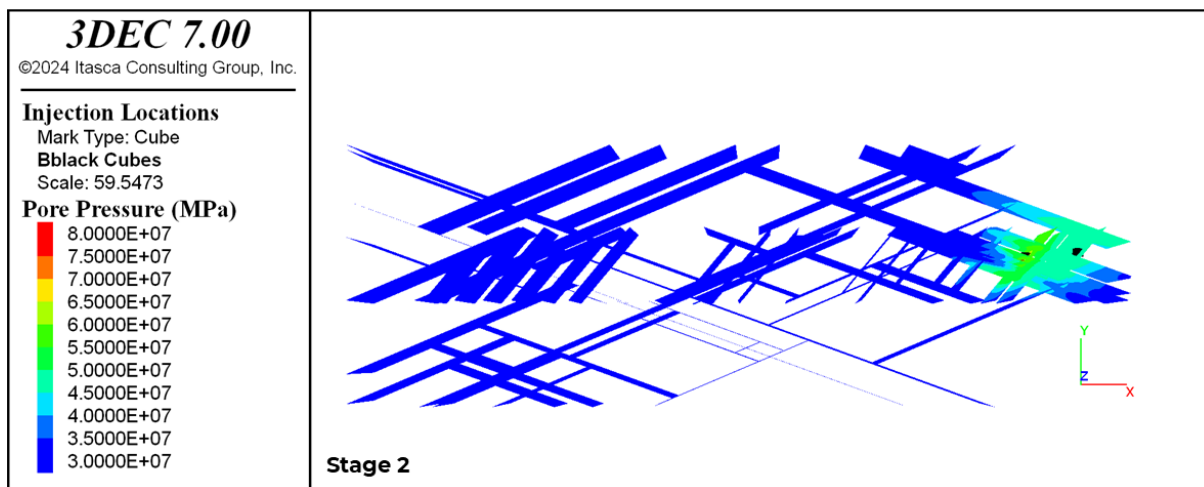
- Pore pressure contour plot to present the diffusion of pressure through the fault and HF network at the end of each stage.
- Pore pressure history graph to observe pressure changes over time.

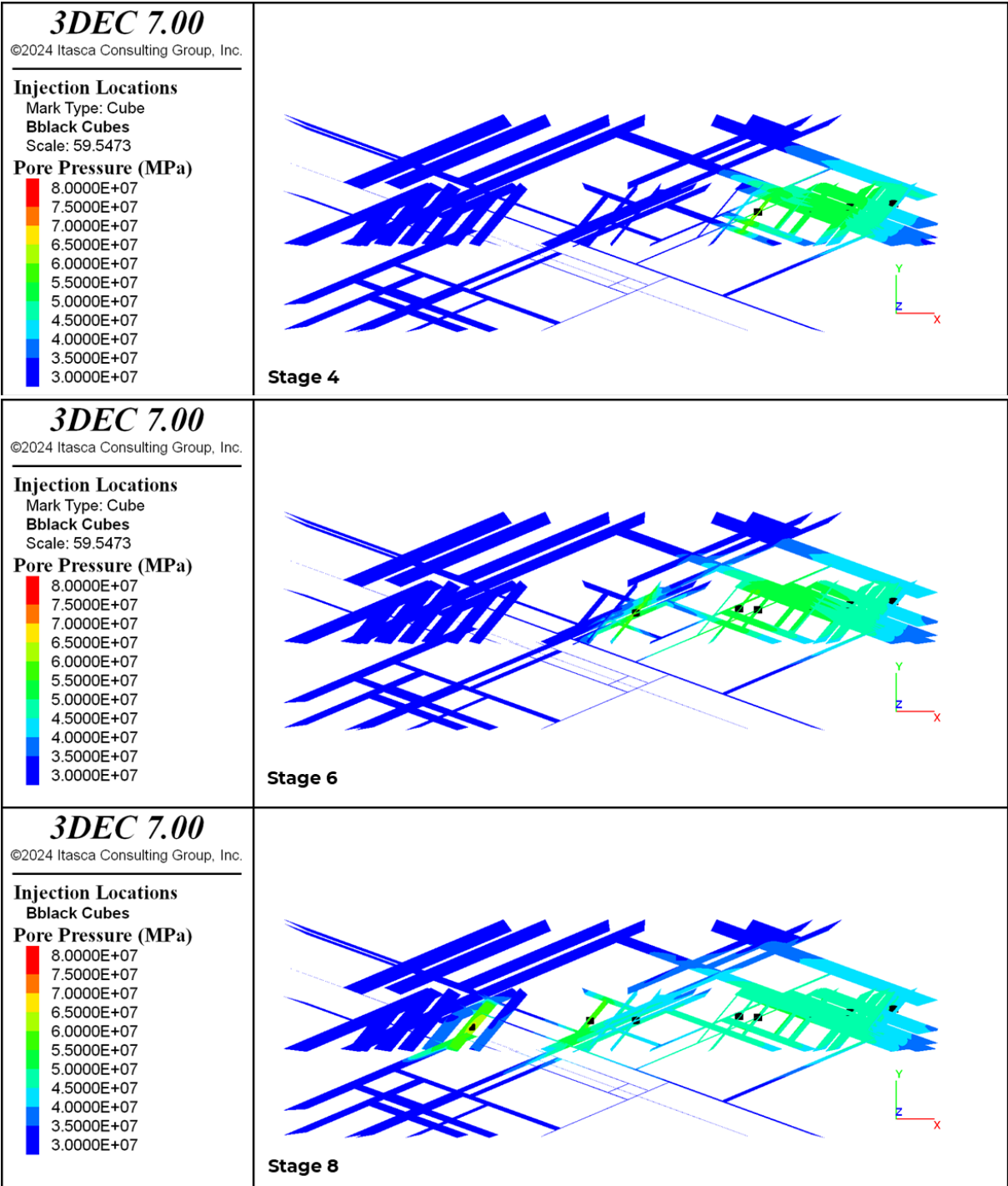
- Seismic moment magnitude scalar plot to present the distribution of induced seismic events.
- Histogram of seismic moment magnitude to offer a comprehensive view of the seismic event distribution and the frequency of occurrence of each magnitude.
- Cumulative frequency plot shows the total number of events with magnitudes greater than or equal to a given value, helping to highlight trends in event occurrence across different magnitude ranges.
- Complementary Cumulative Distribution Function (CCDF) plot to represent the probability of observing a value greater than or equal to a certain threshold in a dataset. In the context of seismic events, the CCDF shows how many events have a magnitude greater than or equal to a specific value. It is the complement of the Cumulative Distribution Function (CDF), which focuses on events less than or equal to a threshold. The CCDF is particularly useful for understanding the rarity of extreme events, such as large earthquakes, compared to more frequent smaller events. The CCDF curve typically decays as the magnitude increases, indicating that fewer large events occur as the magnitude becomes larger. Plotting the log of the CCDF against magnitude helps reveal the underlying relationship between event size and frequency, often following an exponential decay pattern, which is central to seismic hazard analysis. This is provided as a reference to compare the different scenarios in terms of the magnitude.

4.5.1 Base Case Simulations

Creating a representative geometry and defining properties lays the groundwork for the subsequent analyses. The base case configuration presented in Section 4.3. The objective of the base case simulation is to attempt to replicate the broad spatial pattern and magnitude distribution of the induced seismicity. The simulation of the

Figure 4-5 illustrates pore pressure distribution at multiple stages of injection for the base case. Figure 4-6 presents a history of pore pressure over time for the injection points. It shows the maximum pore pressure at the injection point corresponds with the average injection pressure.





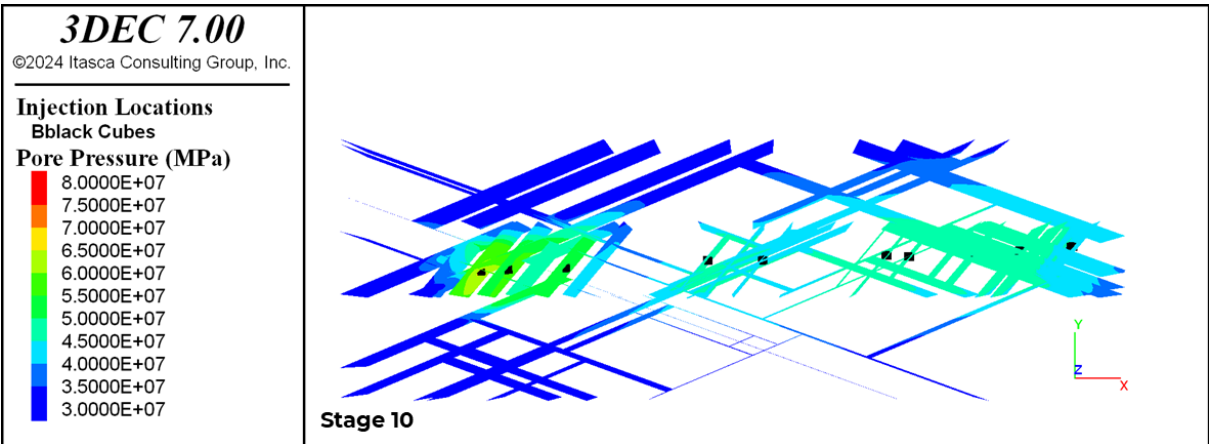


Figure 4-5: Pore Pressure Distribution at the End of Stage 2, 4, 6, 8 and 10 for the Base Case. The Small Black Dots on the Hydraulic Fractures Represent the Injection Points

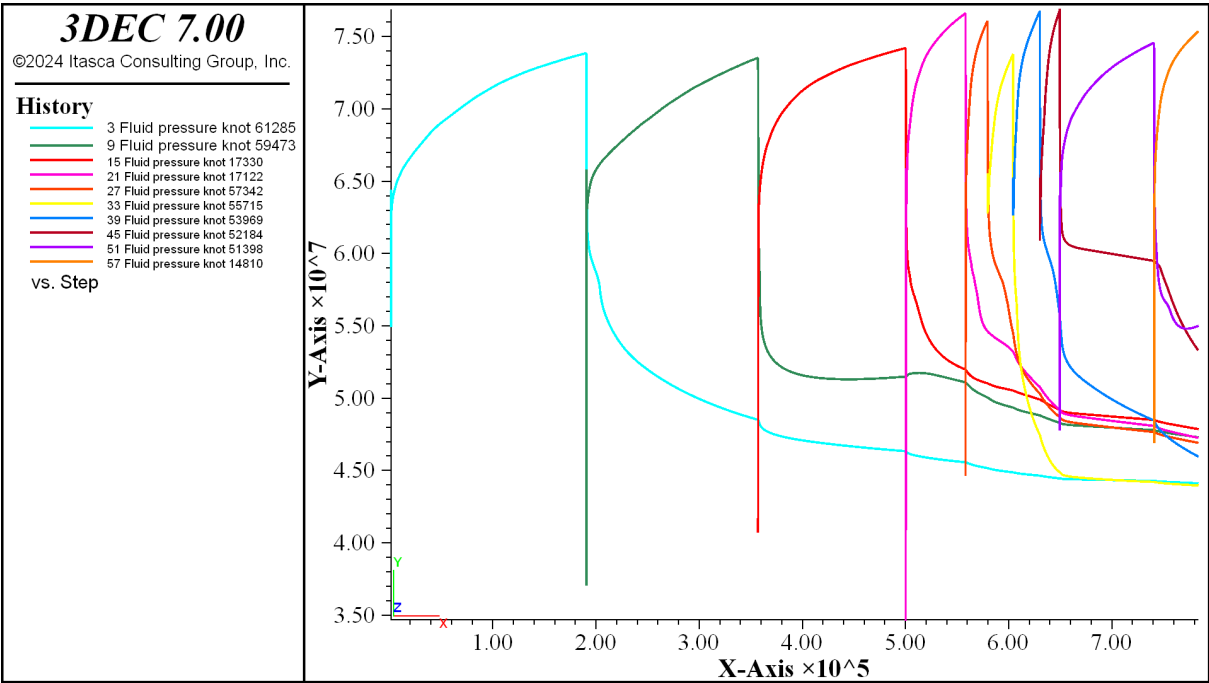


Figure 4-6: Pore Pressure History Graphs at the End of Stage 10 for the Base Case

Figure 4-7 shows a scatter plot of seismic events contoured by magnitude. Micro-seismic events (negative magnitudes) are removed in another figure to better present induced seismic events along the model. It is indicated the seismic events are predominant along HF and NE-SW trending DFN sets.

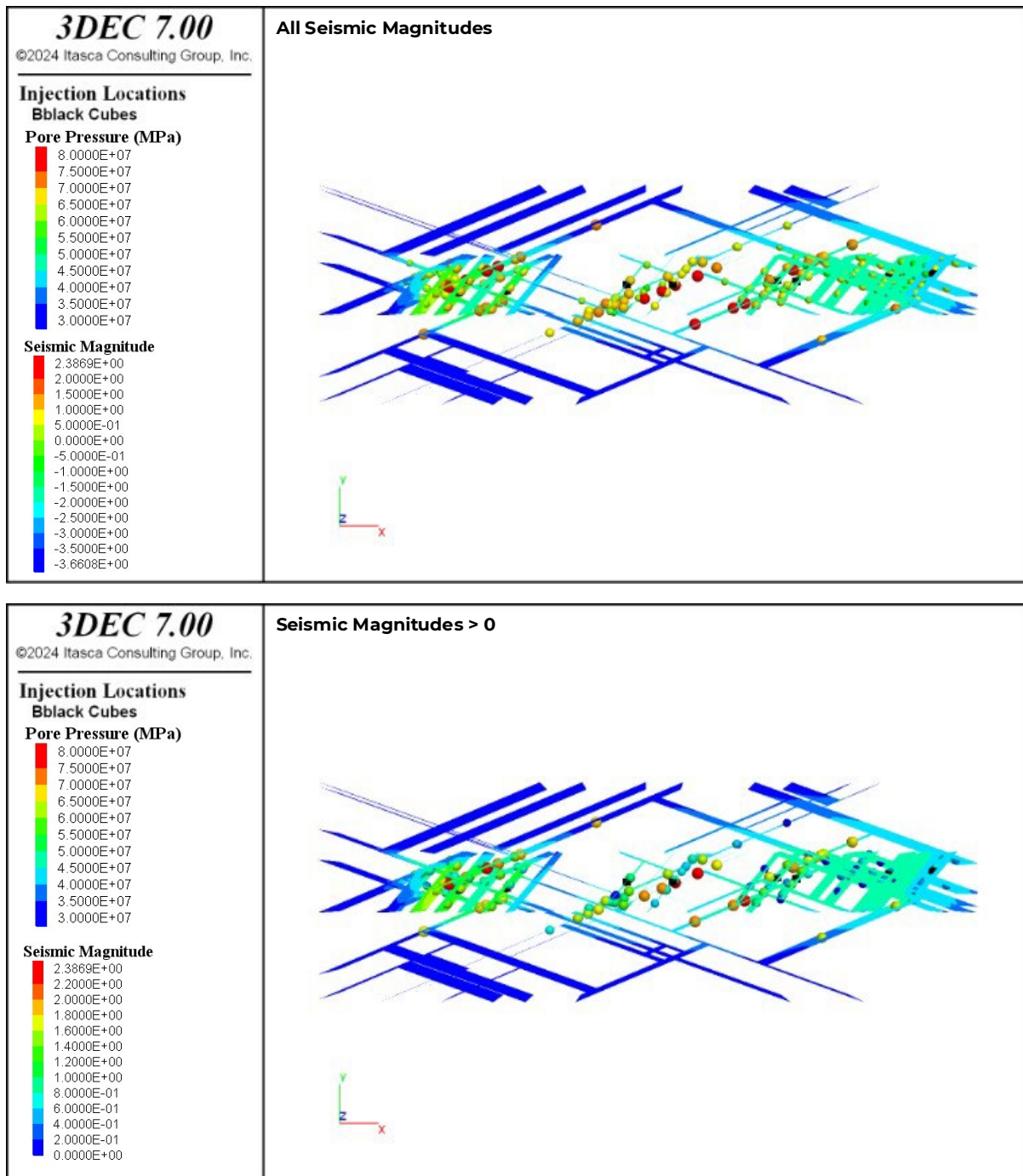


Figure 4-7: Induced Seismicity at the End of Stage 10 of Injection for the Base Case. Top: all Seismic Events; Bottom: Positive Magnitudes

Figure 4-8 presents histogram of moment magnitude which indicates that events with 0.2 and 0.3 magnitudes are the most frequent. The total number of events are reported as 438 with the largest magnitude of 2.39. These results are in agreement with the field observations.

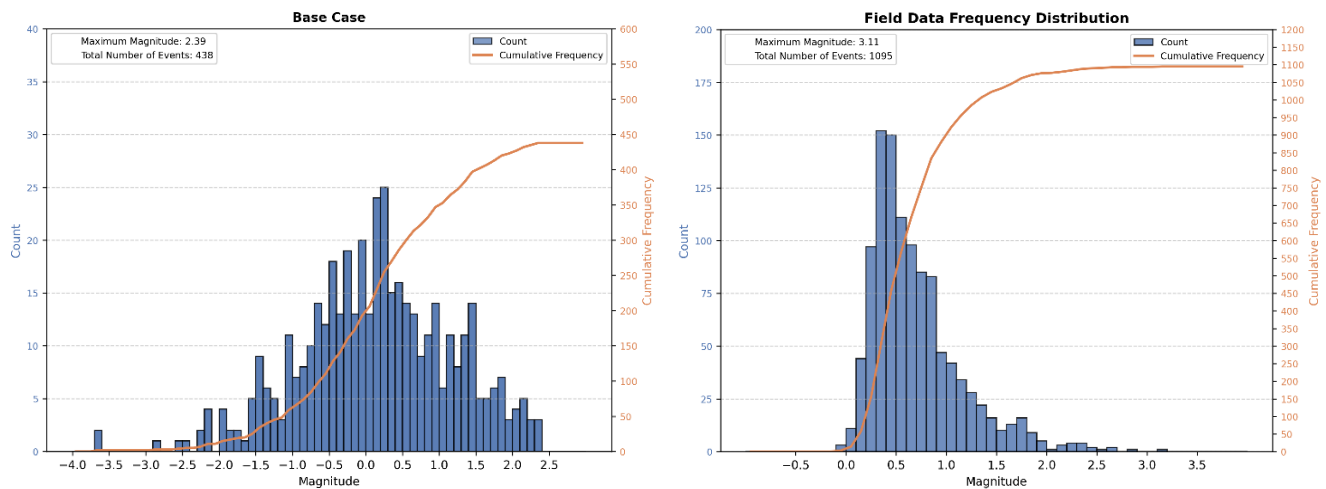


Figure 4-8: Histogram of Moment Magnitude for the Base Case (Left) and Field Data (Right)

Figure 4-9 focuses on events larger than zero. The CCDF curve decreases with increasing magnitude, reflecting the lower frequency of larger events.

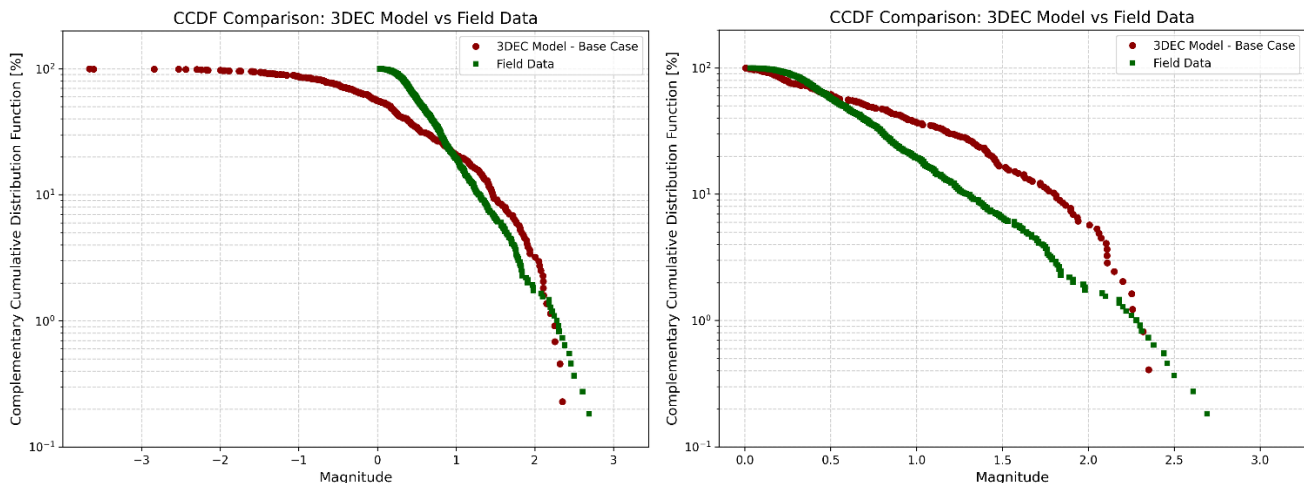


Figure 4-9: Comparison of Measured (Field) and Simulated Seismic Magnitudes. The Left Plot shows the Full Modelled Range, and the Right Plot shows the Modelled Data Clipped to the Minimum Measured Value, Magnitude Zero

4.5.2 Base Case Summary

The base case model has achieved its objectives:

- The range of modelled and measure magnitudes is broadly the same. The maximum modelled magnitude is slightly lower at 2.4 compared to a measured 2.7 but the overall match is reasonable.
- The main seismic events can be seen to be occurring on the NE-SW structures, inferred to be the main seismogenic population from the earlier DFN analysis.

Pressure can be observed moving along the NW-SE structures without any resulting seismicity being generated, confirming the notion that these.

4.5.3 Mitigation Cases

This base case model has subsequently been tested using a number of mitigation strategies in an attempt to reduce the observed seismicity.

Multiple scenarios were developed to examine the influence of different parameters on induced seismicity, and to eventually introduce mitigation strategies. These scenarios involved injection rates, viscosity, length of hydraulic fractures and pressure ramp up time.

4.5.4 Lower Injection Rate

A lower injection rate was set to 75% of the base case, which equals to 0.15 m³/s. Note that, to maintain the same injection volume, the injection time was increased to 3200 s. Note that, all other model parameters remained unchanged. In the analysis, the base case shows a higher number of events than the lower injection rate by 18 events (Figure 4-10). This discrepancy could be attributed to differences in the overall seismic activity generated under the two conditions. The base case likely represents a natural or unaltered seismic environment, where events occur at a higher frequency due to typical stress accumulation and release patterns. In contrast, the lower injection rate may introduce less pressure or stress into the system, resulting in fewer seismic events. Despite this difference in event frequency, the maximum magnitude of the events is similar between the two cases, though the base case still exhibits a slightly higher maximum magnitude (by 0.03). This could indicate that while the base case generates more frequent events, the energy released in individual events is slightly larger, possibly due to different fault or stress behaviors in the natural system compared to the controlled conditions of the injection scenario. This modelling therefore does not indicate that a lower injection rate represents a potential mitigation strategy.

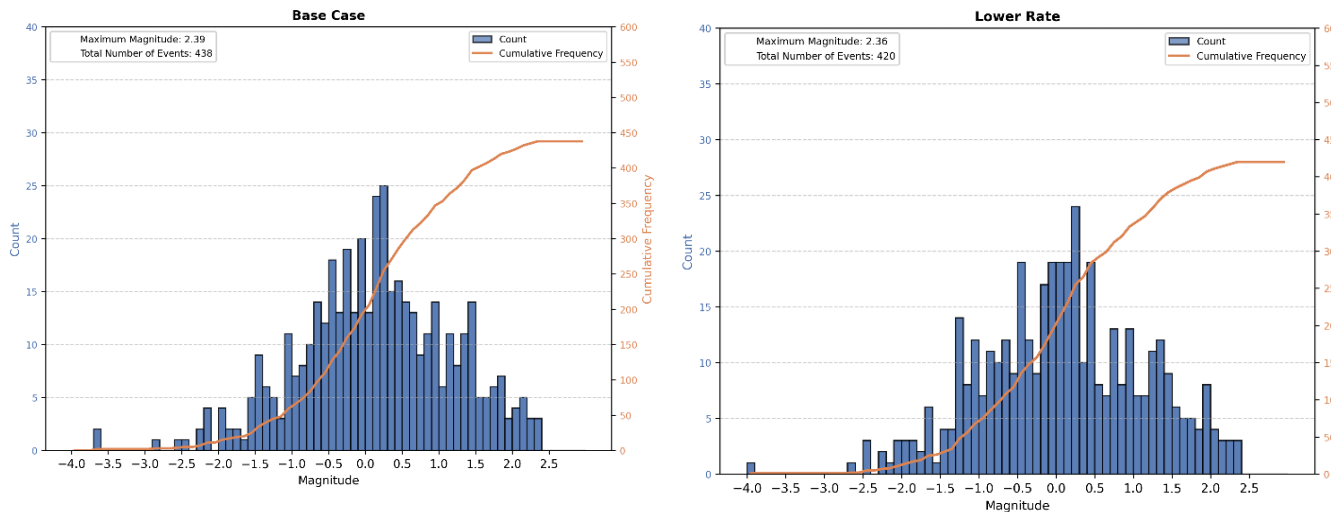


Figure 4-10: Comparison of Seismicity Distribution for the Base Case (Left) and Lower Injection Rate (Right)

4.5.5 Hydraulic Fracture Length Cases

In the two pads considered within this study, one used open hole completions and the other a plug and perf style completion. A key difference between the two styles is often length of the hydraulic fractures, with open hole created hydraulic fractures typically extending further than plug and perf created ones. All the base case modelling scenarios used hydraulic fractures with a half length of 125 m (total length 250 m), consistent with plug and perf completions and operator analysis. The performance of this base case (plug and perf) scenario has been compared against an alternative open hole style completion, where the hydraulic fractures have been extended to a half length of 300 m (total length 600 m). No additional faults were included in the long frac model (Figure 4-11).

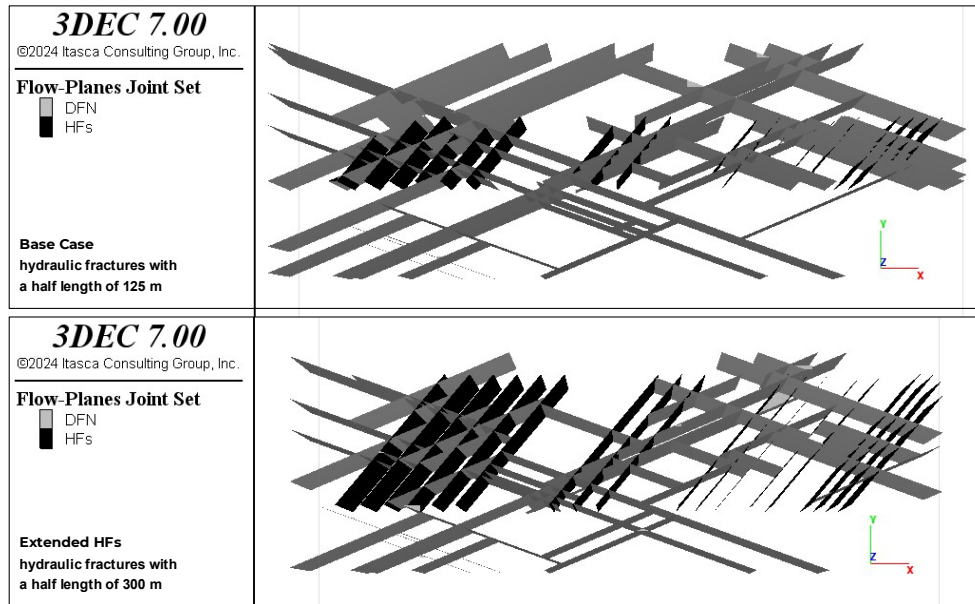


Figure 4-11: Comparison between the Base Case Model (125 m Long Fracs) and Extended Frac Model (300 m Long Fracs)

Figure 4-12 presents seismic event distributions for these two cases. According to this figure:

- The model with extended fractures has slightly more events, suggesting a marginal increase in overall seismic activity.
- Both scenarios show nearly identical maximum magnitudes.
- The Base Case shows a slightly broader distribution with more events at positive magnitudes. The model with extended fractures has a more symmetric distribution centered around ~ -0.5 to 0.5 , with a slightly higher count of smaller-magnitude events (-2.0 to 0.0).
- This modelling therefore does not indicate that HF length represents a key risk from the perspective of induced seismicity.

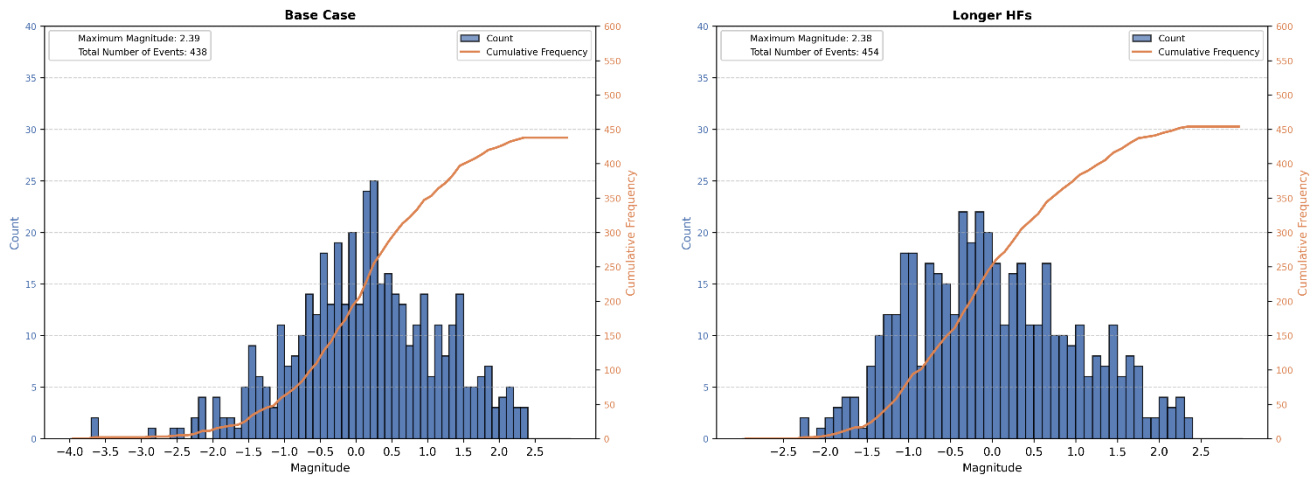


Figure 4-12: Comparison between the Seismicity for the Base Case Models (125 m Long Fracs) and Extended Frac Model (300 m Long Fracs)

4.5.6 Slower Ramp up

There is some evidence that increasing the time over which pumping reaches its maximum pump rate (i.e., a slower ramp up rate), may reduce the amount of induced seismicity. To test this, the base case model has been compared against 5 scenarios with different ramp up rates. The following assumptions and steps were used to estimate the ramp-up rate:

- The injection time was represented by number of computing cycles.
- Flux was calculated by dividing the total injected volume by the injection duration (either time or total number of cycles).
- Twenty percent of the total cycles was allocated for ramp-up; this is referred to as the *ramp-up cycles*.
- The injection rate during ramp-up was calculated by dividing the total flux by the number of ramp-up cycles. This value represents the incremental increase in injection rate per cycle during the first 20% of the total cycles.
- The injected volume during ramp-up was then estimated by multiplying the ramp-up injection rate by the ramp-up cycles.
- Finally, the number of cycles required to inject the remaining volume was calculated.

As an example, for the first scenario it was assumed that the total number of cycles is 1800. In that case:

- Total injection volume = 480 m³
- Flux = Cycles / Total Injection Volume = 0.26667 cycles/m³
- Ramp-up cycles = 0.2 × 1800 = 360 cycles
- Ramp-up rate = Ramp-up cycles / Flux = 0.00074 m³/cycles
- Ramp-up injected volume = Ramp-up rate × (Ramp-up cycles)² / 2 = 48
- Remaining number of cycles = (Total Injection Volume – Ramp-up injected volume) / Flux = 1620 cycles

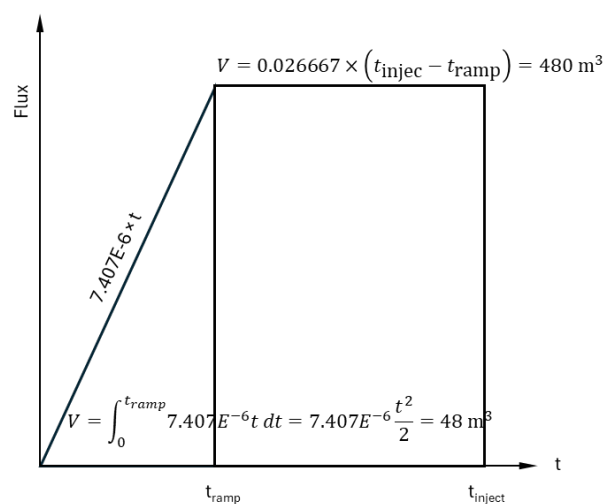


Figure 4-13: The Concept of Flux vs Injection Duration for the Ramp-up Scenarios

The same approach was adopted for the other scenarios which are listed in Table 7. Note that all other parameters in the model remained the same.

A comparison of the ramp-up rate, maximum flow rate and duration of pumping is shown in Figure 4-14 for all scenarios. In all cases, the total volume injected is the same.

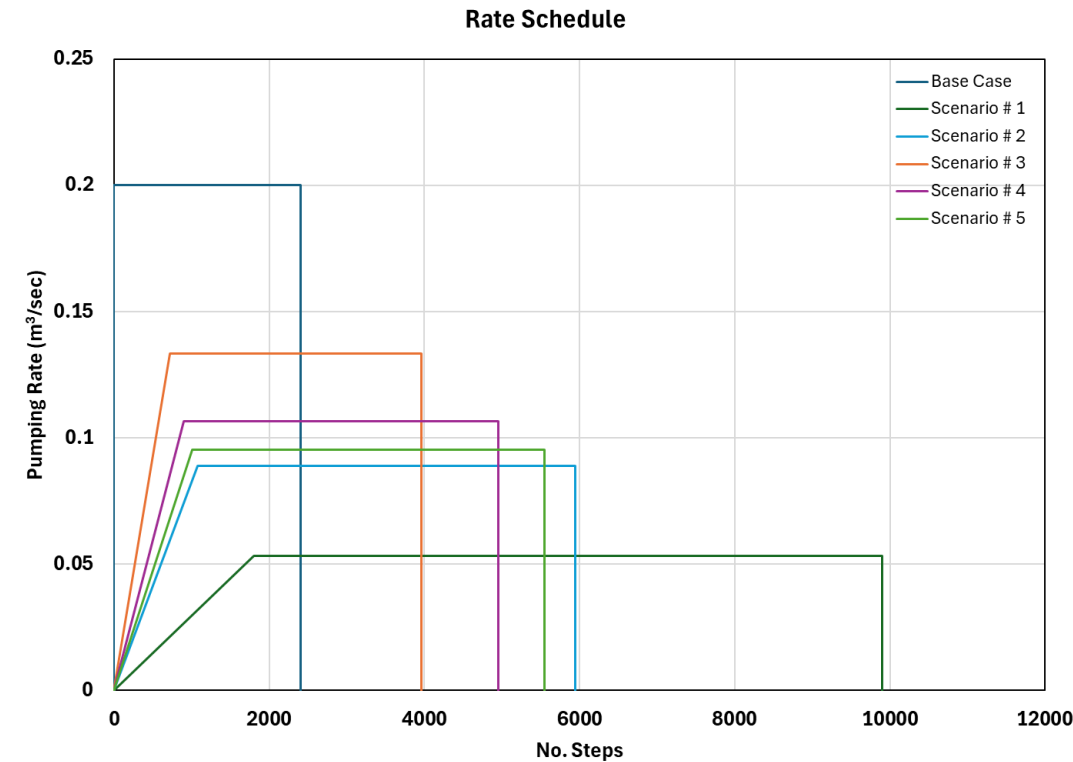
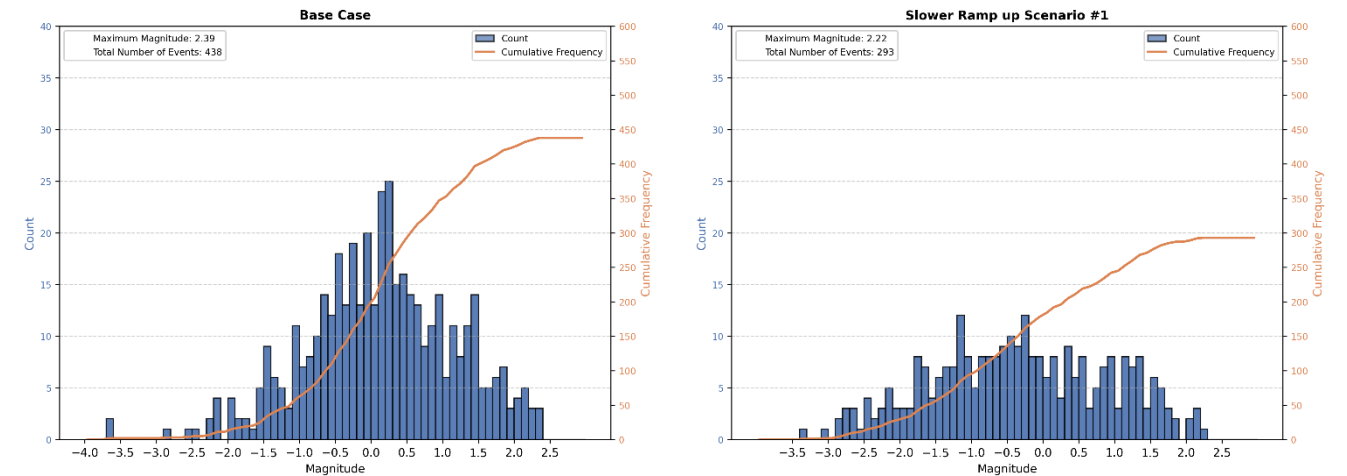


Figure 4-14: Ramp-up Rates and Pumping Durations

Table 7: Base Case and 5 Different Ramps up Scenarios

| Scenario | Number of Cycles to Full Rate |
|----------------------|-------------------------------|
| Base Case Model | 18000 |
| Ramp up Scenario # 1 | 360 |
| Ramp up Scenario # 2 | 720 |
| Ramp up Scenario # 3 | 1800 |
| Ramp up Scenario # 4 | 1080 |
| Ramp up Scenario # 5 | 900 |

In the comparison between the base case and five different slower ramp-up scenarios (Figure 4-15), all of the lower ramp-up scenarios show a significantly lower number of events compared to the base case. This suggests that a more gradual increase in injection rate reduces the frequency of seismic events, possibly due to more controlled stress accumulation over time. Among the ramp-up scenarios, Scenario #1 exhibits the highest number of events, indicating that the initial stages of the ramp-up may still trigger a noticeable amount of seismic activity. Scenario #3 has the lowest number of events, which could reflect a slower or more gradual stress release that leads to fewer seismic occurrences. Additionally, the maximum magnitude of events in Scenario #3 is the lowest, reinforcing the idea that a slower ramp-up may limit the intensity of individual events, likely due to less rapid energy buildup in the system compared to the other scenarios.



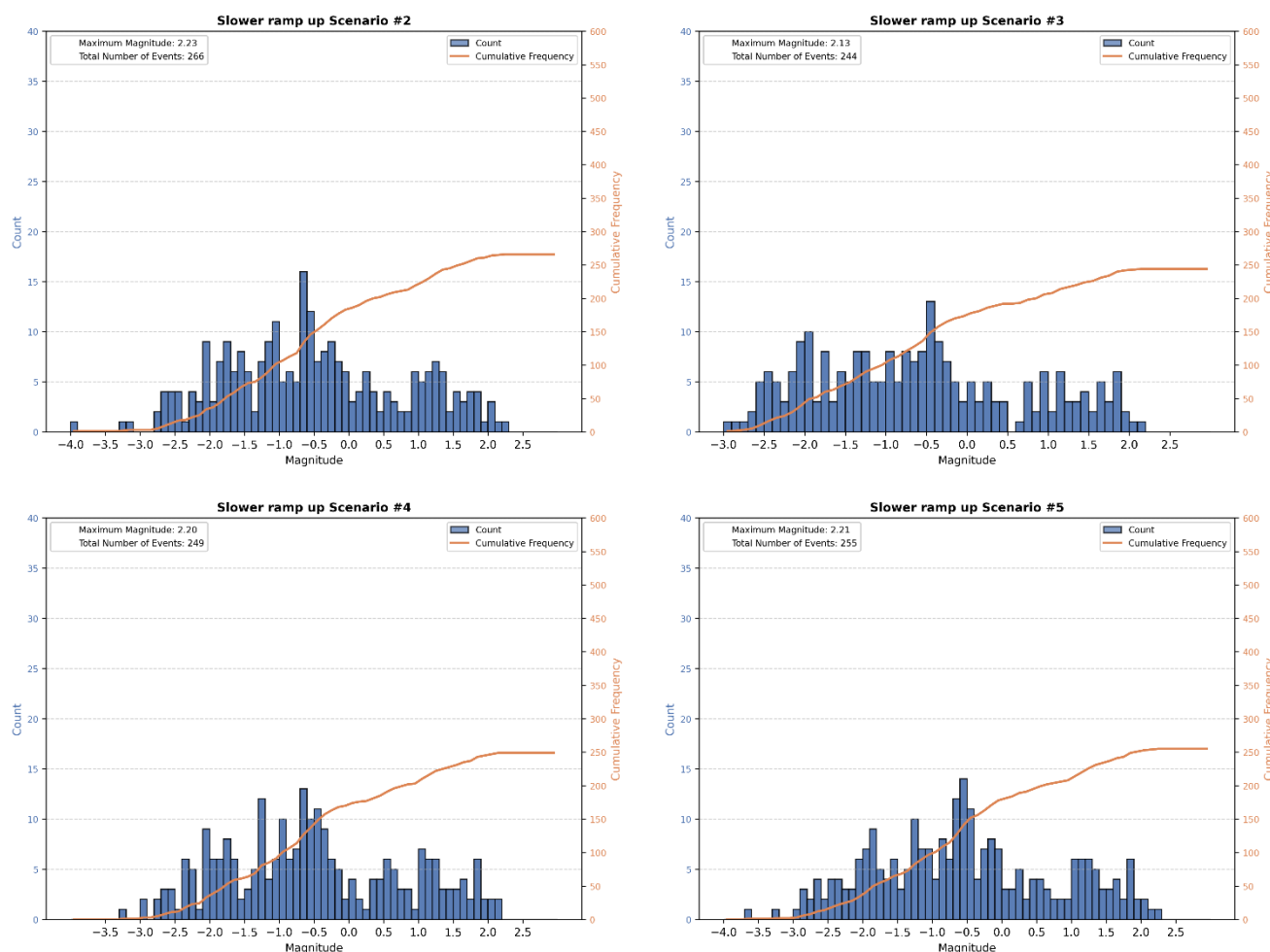


Figure 4-15: Comparison of Seismicity Distribution for the Base Case and 5 Different Ramp up Scenarios

4.5.7 Increased Viscosity

Viscosity is a measure of a fluid's resistance to flow with a water having a viscosity of around 1 cp (0.001 Pa.s). The thicker the fluid, the higher the viscosity. With increasing viscosity, fluid finds it harder to migrate through complex fracture networks and there is some evidence that employing higher viscosity fluids, may help mitigate induced seismicity. To test this, three different scenarios have been considered, which are listed in Table 8. These three scenarios represent the use of a base case low viscosity fluid consistent with a standard slick water frac, a medium viscosity fluid consistent with a high concentration of polyacrylamide additive and a high viscosity fluid consistent with a cross linked gel.

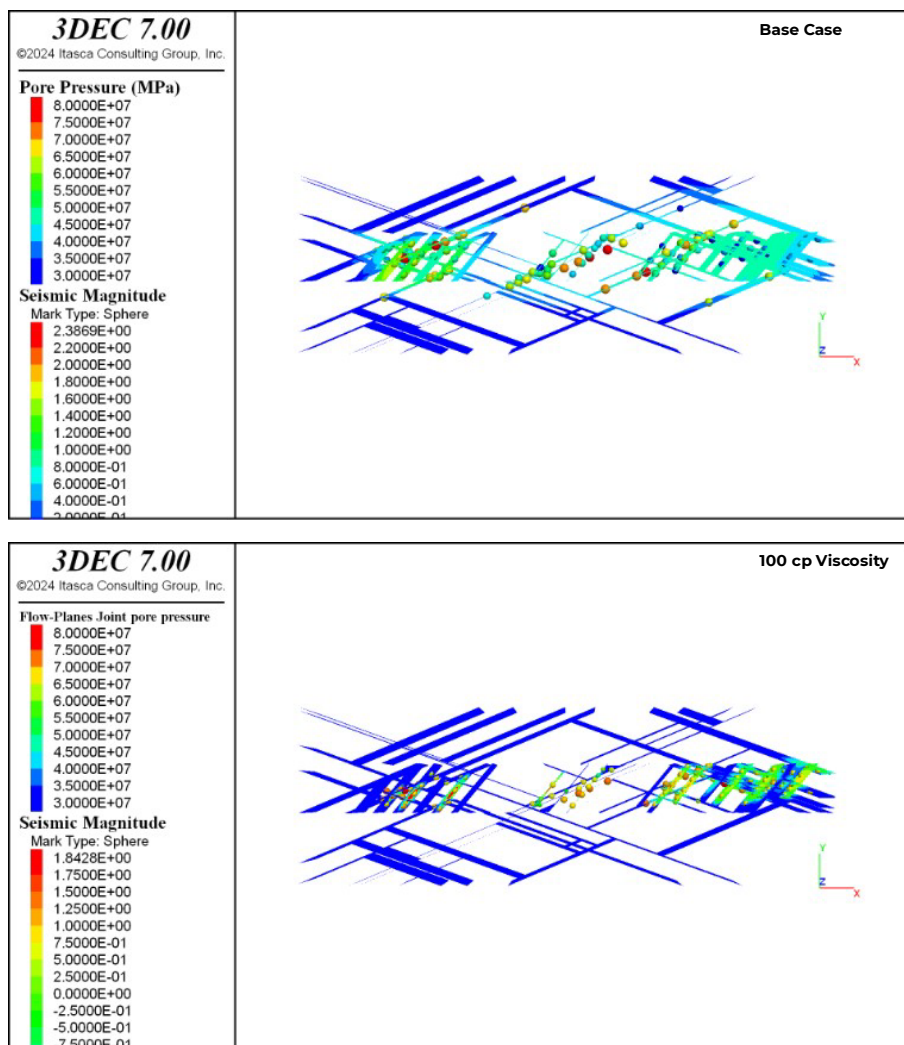
Table 8: Viscosity Cases

| Viscosity case | Additive | Achievable viscosity (cp) |
|--------------------------|--|---------------------------|
| Low viscosity- base case | Slickwater frac with low friction reducer | 2 cp |
| Medium viscosity case | High polyacrylamide friction reducer concentration | 100 cp |
| High viscosity case | Cross-linked gels | 300 cp |

Images of the three models can be seen in Figure 4-16. These show a number of clear trends over the three models:

- The perturbation of pore pressure is seen to be more restricted with increasing viscosity, with limited pressure change being noted at distance.
- Associated with this reduction in pore pressure change, there is a clear reduction in the number of larger events seen developing on the NE-SW seismogenic structures. This trend suggests that higher viscosity may increase the frictional resistance within the system, leading to less seismic activity. Furthermore, the decrease in maximum magnitude indicates that the events triggered under higher viscosity conditions tend to be less intense, likely due to the smoother and more gradual nature of stress release facilitated by the higher fluid viscosity.
- The events are being increasingly focussed within the hydraulic fractures and close to the wells

Histograms of the event magnitude distribution for the three scenarios are shown in Figure 4-17. These show that both the number of events and the maximum magnitude show are decreasing with increasing viscosity.



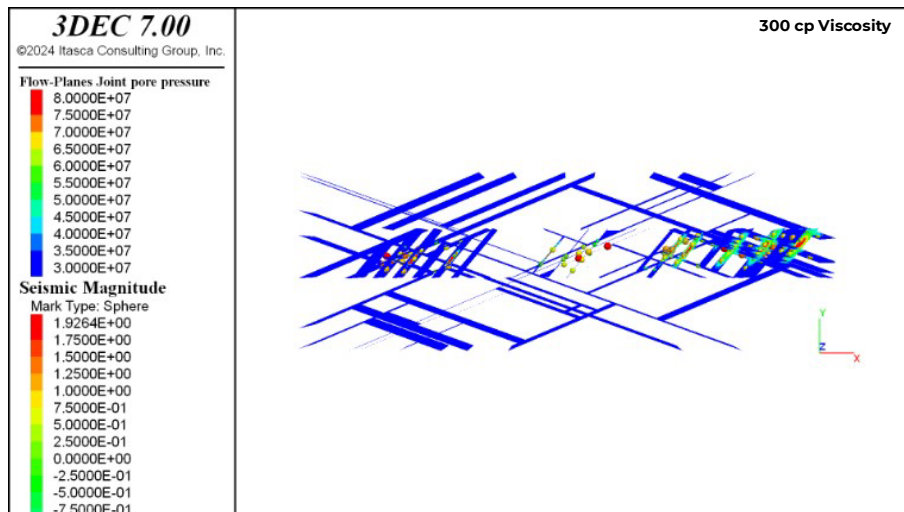


Figure 4-16: Comparison of the Induced Seismicity Distribution for the Base Case and 2 Different Viscosity Scenarios

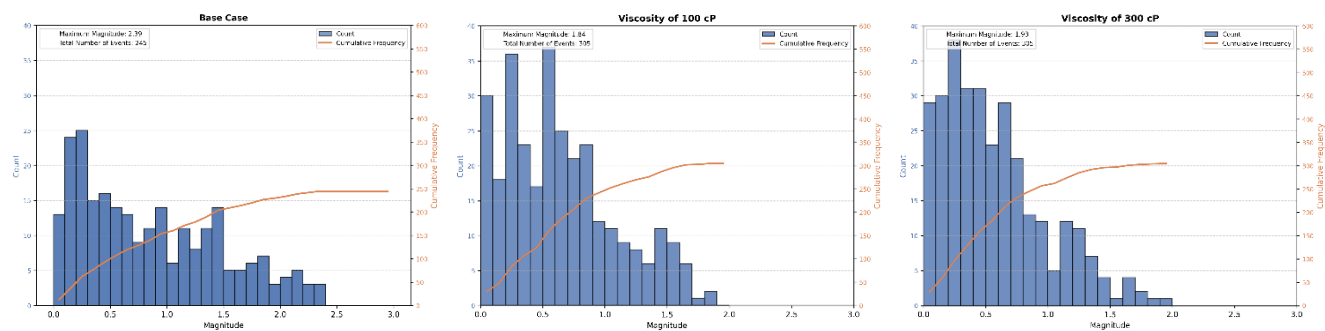


Figure 4-17: Comparison of Seismicity Distribution for the Base Case and 2 Different Viscosity Scenarios. Modelled Magnitudes only Displayed about Magnitude

4.6 Summary of Numerical Assessment

Figure 4-18 and Figure 4-19 summarizes the total number of events for and the largest moment magnitude for the base case and other scenarios. It is indicated that the number of induced events varies significantly across the different injection scenarios. Figure 4-20 summarizes the seismicity distribution for all scenarios.

Scenario #3, which features a slower ramp-up rate, resulted in the lowest number of events, with only 244 recorded. This is likely due to the more gradual increase in injection pressure, allowing the formation to adjust more steadily and reducing the likelihood of abrupt stress changes that typically trigger seismicity. In contrast, the scenario involving longer hydraulic fractures (HFs) generated the highest number of events, with a total of 454. The extended fracture networks likely provided greater connectivity and surface area for fluid interaction, thereby increasing the potential for fault activation and microseismic activity. Regarding that the Scenario #3 resulted in the fewest events, it also produced one of the lowest maximum magnitudes at 2.13. The highest recorded magnitude overall was observed in the base case at 2.39, closely followed by the longer HFs scenario, which reached a maximum magnitude of 2.38. This suggests that while the number of events is influenced by injection style and fracture extent, the maximum magnitude may be more sensitive to the specific fault activation conditions within each scenario.

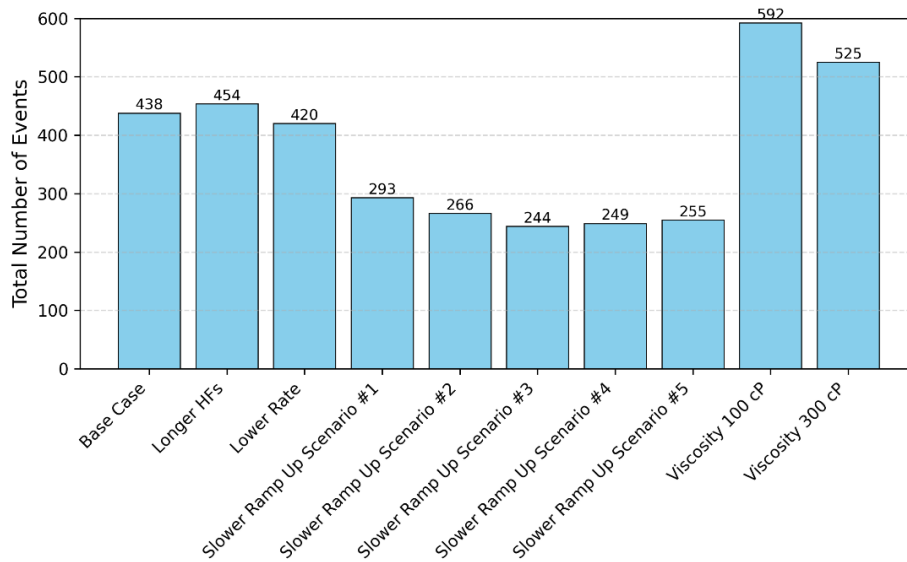


Figure 4-18: The Comparison of the Number of Events in Each Scenario

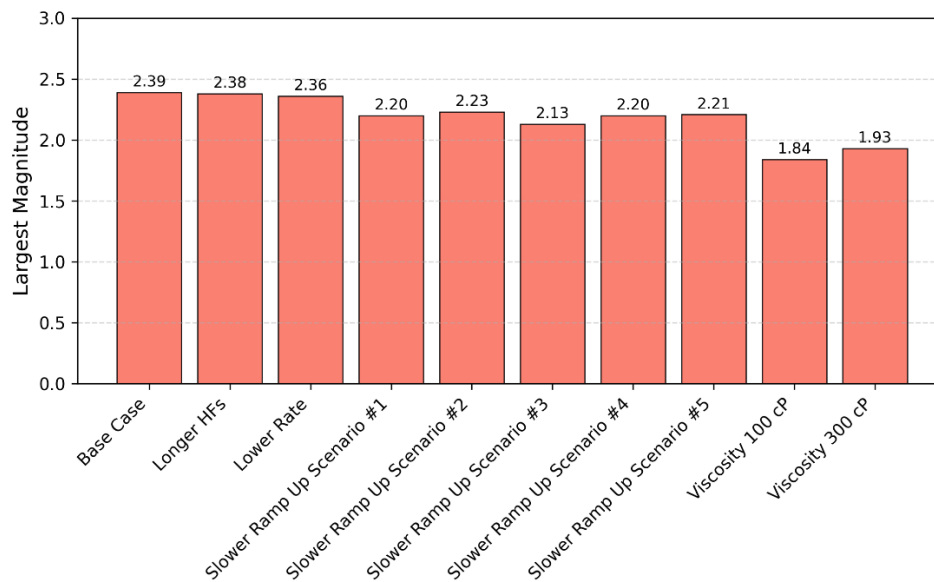


Figure 4-19 The comparison of the Largest Magnitude in Different Scenarios

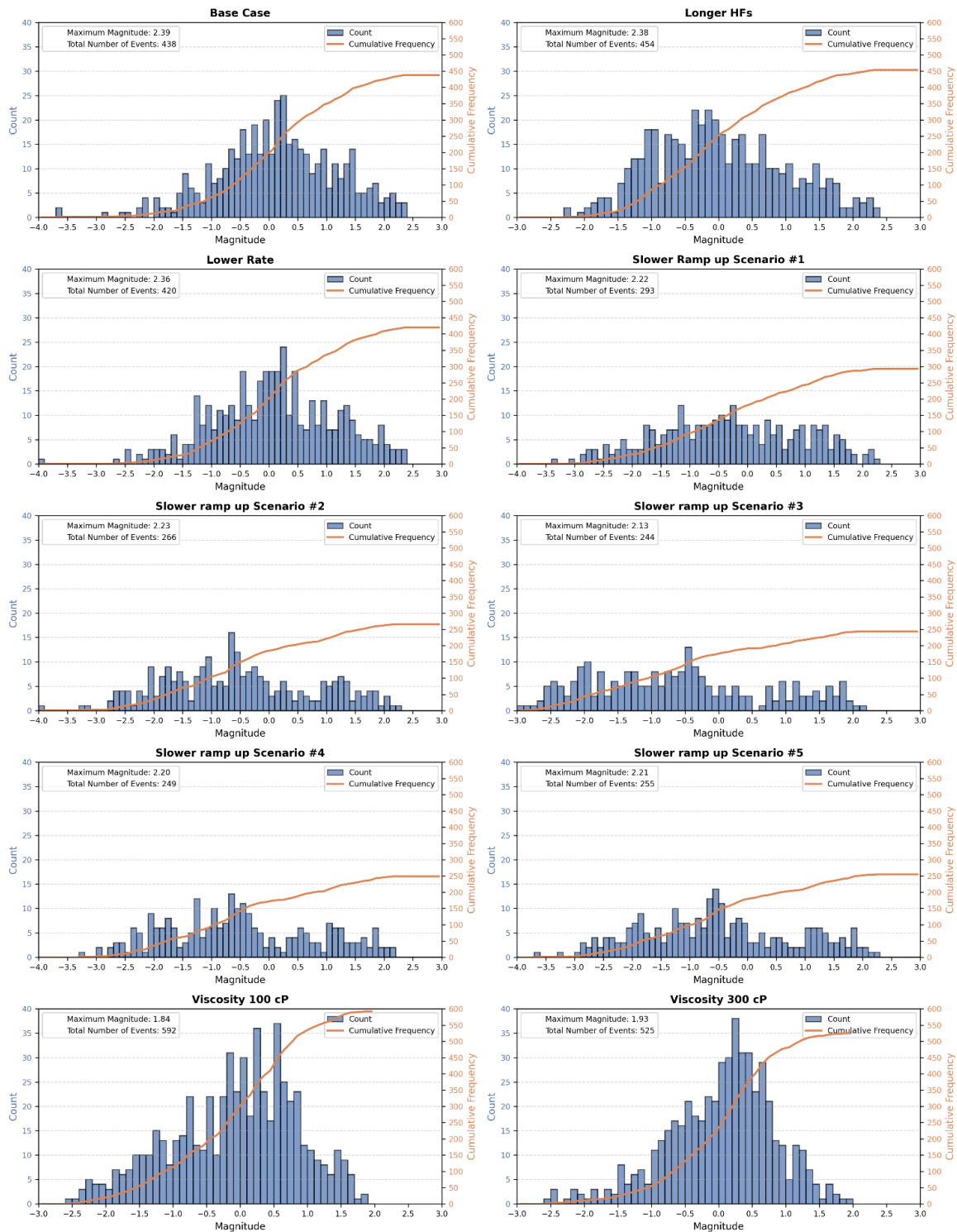


Figure 4-20: Summary of Seismicity Distribution for the Base Case and all other Scenarios

5.0 SUMMARY

Data Review

Analysis of the two adjacent induced seismic data sets (2022 and 2024) shows both similarities and differences between the two data sets:

- The distribution of magnitudes shows quite different patterns between the open hole and cased wells although they both show the same maximum magnitude. It is believed that the engineered “cased hole” completion results in a generally narrow range of magnitudes although the fault system itself strongly influences the maximum magnitude.
- The orientation of the induced lineaments for the 2022 dataset and 2024 dataset are within ~4 degrees (063 v 067 respectively), suggesting a very similar pattern of structures exist over a scale of >2 km, the distance between the two pads.
- The size distribution of induced lineaments from both datasets, all show a very similar trend, with a power law slope of -1. This also suggests a similar pattern of structures are being stimulated over this multi-pad scale.
- When the size distribution of the TGS seismic faults is added to the same power law plot, these faults have an almost identical gradient to the induced lineaments. Whilst there is some ambiguity about the normalisation area, it appears the intensity of the induced seismic lineaments is well aligned with the larger scale TGS seismic faults. We infer because of this power law relationship between the larger seismic structures and the smaller induced lineaments, that they are genetically related (i.e., the induced structures represent the smaller length range of the mapped seismic faults). ***This relationship has potential for pre-stimulation understanding of the fault system.***
- The interpreted maximum horizontal stress orientation for the two pads shows some difference with 028 degrees for the 2022 dataset and 040 degrees for the 2024 dataset. The confidence in the 2022 SHmax direction is relatively low so it is considered that these two values are in broad agreement.

DFN Analysis

The DFN modelling of the 2024 data set has achieved the following:

- The DFN modelling has confirmed that there a district scale structural fabric presumed to be associated with the nearby Fort St John graben, that can be seen at the 2022 and 2024 pads, some 2 km apart. That is, this is not just a pad scale phenomenon.
- The DFN analysis has inferred the reservoir fault fabric by reproducing induced seismicity through the identification of connected NE-SW seismogenic structures and inferred NW-SE aseismogenic faults. This basic conceptual model has been shown to reproduce the broad spatial pattern of events including the distribution of the distance of the events from the well.
- Unlike previous work where this modelling used a brute force manual optimisation, this optimised matching has been achieved using the PEST code (Parameter Estimation).
- The results from the 2024 data set are very similar to 2022 analysis, again indicating that the structural pattern at the two pads is inferred to be the same.

- Using the DFN model to investigate changes in the connected population as a function of hydraulic fracture length. These results showed that the longer (open hole) fracs result in potential seismicity extending a little further away from the well (P80 distance for 150 m fracs 500 m, and 600 m for 600 m fracs). However, the longer fracs do result in the increased connection to reservoir fractures (both count and total area) and it is believed that this does increase the seismic potential of open hole stimulation relative to shorted plug and perf fracs.

3DEC numerical simulations

The 3DEC simulations have confirmed the conceptual model exploited by the DFN model, namely:

- The main seismic events can be seen to be occurring on the NE-SW structures, inferred to be the main seismogenic population from the earlier DFN analysis.
- In addition to the NE-SW structures, pressure can be observed moving along both the NW-SE structures without any resulting seismicity being generated, confirming the notion that these represent an aseismogenic population of structures.
- The broad distribution of simulated induced seismic magnitudes is in reasonable agreement with the observed seismic magnitudes suggesting that the base case model represents a reasonable description of the actual sub-surface system.

This base case model was subsequently used to test a number of potential mitigation strategies:

- The injection rate was reduced to 75% of the base case—**No impact.**
- Slower ramp up to injection pressure—**Seismicity reduced.**
- Hydraulic fracture length—**Longer fracs resulted in slightly more seismicity.**
- Injection fluid viscosity—**Reduction in higher magnitude events with more smaller events being generated close to the well.**

6.0 CLOSURE

The reader is referred to the Study Limitations section (after Executive Summary), which precedes the text and forms an integral part of this report.

If you have any questions or comments, please contact the undersigned.

Signature Page

WSP Canada Inc.



Yaniv Fogel

Experienced Rock Mechanics Specialist



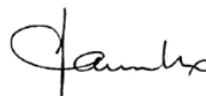
Steve Rogers

Principal Geoscientist – Senior



Athena Pirayehgar

Mining Specialist



Joe Carvalho

Rock Mechanics Expert – Mining Engineering

YF/SR/AP/JC/hm/ah

[https://wsponlinecan.sharepoint.com/sites/ca-2023ca121088/shared documents/06. deliverables/working/final report - 003/final - rev0/2023ca121088-003-r-rev0-ogris induced seismicity report 15jul_25.docx](https://wsponlinecan.sharepoint.com/sites/ca-2023ca121088/shared%20documents/06.%20deliverables/working/final%20report%20-%20003/final%20-%20rev0/2023ca121088-003-r-rev0-ogris%20induced%20seismicity%20report%2015jul_25.docx)

REFERENCES

- Davy, P. 1993. "On the Frequency-Length Distribution of the San Andreas Fault System." *Journal of Geophysical Research: Solid Earth* 98 (B7): 12141–51. <https://doi.org/10.1029/93JB00372>.
- Dreuzy, J.-R. de, P. Davy, and O. Bour. 2002. "Hydraulic Properties of Two-Dimensional Random Fracture Networks Following Power Law Distributions of Length and Aperture." *Water Resources Research* 38
- Hanks, T.C., and Kanamori, H. 1979. A Moment Magnitude Scale. *Journal of Geophysical research*, 84(9): 2348–2350.
- Itasca Consulting Group Inc. 2025. 3DEC: version 7.00.
- S. McKean, S. Rogers, J.A. Priest, J. Dettmer. 2024. In Press. Inferring Hydrostructural Fracture Architecture from Induced Seismic and Microseismic Point Clouds. *Rock Mechanics & Rock Engineering*.
- Steve Rogers & Scott McKean. 2022. Integrating Induced Seismicity Observations and Discrete Fracture Network Modelling to Characterize the Natural Fracture Architecture of the Montney Formation, British Columbia. *Proceedings of the 10th Unconventional Resources Technology Conference. WSP 2023. Modelling and Analysis of KSMMA - Induced Seismic Events to Advance Event Mitigation Strategies. Report for BC OGRIS.*

